Monthly Notices
of the
ROYAL ASTRONOMICAL SOCIETY

MNRAS **457,** 1419–1446 (2016) doi:10.1093/mnras/stv2987

The GHOSTS survey – II. The diversity of halo colour and metallicity profiles of massive disc galaxies*

Antonela Monachesi,[1]† Eric F. Bell,[2] David J. Radburn-Smith,[3] Jeremy Bailin,[4,5] Roelof S. de Jong,[6] Benne Holwerda,[7] David Streich[6] and Grace Silverstein[4]

[1]*Max Planck Institute for Astrophysics, Karl-Schwarzschild-Str. 1, D-85748 Garching, Germany*
[2]*Department of Astronomy, University of Michigan, 311 West Hall, 1085 South University Ave, Ann Arbor, MI 48109, USA*
[3]*Department of Astronomy, University of Washington, Seattle, WA 98195, USA*
[4]*Department of Physics and Astronomy, University of Alabama, Box 870324, Tuscaloosa, AL 35487, USA*
[5]*National Radio Astronomy Observatory, PO Box 2, Green Bank, WV 24944, USA*
[6]*Leibniz-Institut für Astrophysik Potsdam, D-14482 Potsdam, Germany*
[7]*University of Leiden, Sterrenwacht Leiden, Niels Bohrweg 2, NL-2333 CA Leiden, the Netherlands*

Accepted 2015 December 22. Received 2015 November 27; in original form 2015 July 13

ABSTRACT

We study the stellar halo colour properties of six nearby massive highly inclined disc galaxies using *Hubble space telescope* Advanced Camera for Surveys and Wide Field Camera 3 observations in both *F*606*W* and *F*814*W* filters from the GHOSTS (Galaxy Halos, Outer disks, Substructure, Thick disks, and Star clusters) survey. The observed fields probe the stellar outskirts out to projected distances of ∼50–70 kpc from their galactic centre along the minor axis. The 50 per cent completeness levels of the colour–magnitude diagrams are typically at 2 mag below the tip of the red giant branch (RGB). We find that all galaxies have extended stellar haloes out to ∼50 kpc and two out to ∼70 kpc. We determined the halo colour distribution and colour profile for each galaxy using the median colours of stars in the RGB. Within each galaxy, we find variations in the median colours as a function of radius which likely indicates population variations, reflecting that their outskirts were built from several small accreted objects. We find that half of the galaxies (NGC 0891, NGC 4565, and NGC 7814) present a clear negative colour gradient in their haloes, reflecting a declining metallicity; the other have no significant colour or population gradient. In addition, notwithstanding the modest sample size of galaxies, there is no strong correlation between their halo colour/metallicity or gradient with galaxy's properties such as rotational velocity or stellar mass. The diversity in halo colour profiles observed in the GHOSTS galaxies qualitatively supports the predicted galaxy-to-galaxy scatter in halo stellar properties, a consequence of the stochasticity inherent in the assembling history of galaxies.

Key words: galaxies: evolution – galaxies: haloes – galaxies: photometry – galaxies: spiral – galaxies: stellar content.

1 INTRODUCTION

In the Λ cold dark matter (ΛCDM) paradigm, galaxies form in potential wells defined by dark matter haloes (e.g. White & Rees 1978). These haloes grow in great part by the merging of smaller subhaloes plus the kinematic heating of disc stars. This produces a diffuse stellar halo around most galaxies with a structure intimately tied to the growth and assembly history of the system.

Over the past decade, different approaches have been used to observe stellar haloes, a challenging task due to their faint surface brightnesses. Long-exposure wide-field imaging with photographic plates (Malin & Carter 1980; Malin & Hadley 1997) and with small telescopes and wide-field CCDs (e.g. Zheng et al. 1999; Martínez-Delgado et al. 2010) has allowed panoramic mapping of the brightest overdensities in nearby galaxies, revealing numerous tidal streams. Evidence of stellar halo substructures (e.g. stellar streams, shells, etc.) in the outer regions of galaxies was possible with these types of

*Based on observations made with the NASA/ESA *Hubble Space Telescope*, obtained at the Space Telescope Science Institute, which is operated by the Association of Universities for Research in Astronomy, Inc., under NASA contract NAS 5-26555.

†E-mail: antonela@mpa-garching.mpg.de

images, proving the importance of merging in the galaxy formation process. On the other hand, stacks of a large number of similar galaxies allows us to both reach very low surface brightness limits and study the average properties of stellar haloes as a function of certain galaxy parameters, such as halo mass, stellar mass, or bulge-to-disc ratio (e.g. Zibetti, White & Brinkmann 2004; D'Souza et al. 2014). However, none of these techniques allow for a detailed study of the physical properties of individual haloes predicted by models, such as their age and metallicity as a function of galactocentric distance. Integrated light observations are subject to degeneracies between age, metallicity, and extinction as well as being limited in sensitivity due to the sky brightness, flat-field, and scattered light corrections (de Jong 2008). Even using optics with very low scatter light (van Dokkum, Abraham & Merritt 2014), it is not possible to obtain detailed population age and metallicity information.

A more informative but observationally intensive approach for characterizing the properties of nearby galactic stellar haloes is to study their resolved stellar populations. It is possible to measure stellar densities of resolved stars reaching equivalent surface brightnesses as faint as $\mu_V \sim 33$ mag arcsec^{-2}, as well as measuring the stellar populations of those haloes, which is crucial for testing model predictions (Monachesi et al. 2013). One such prediction is that there should be stellar population variations within a halo since the stellar population of haloes should reflect the various satellites that form them. In particular, how a halo has formed and evolved is expected to leave strong imprint on its metallicity or abundance pattern (e.g. Font et al. 2006a; Tumlinson 2010; Cooper et al. 2010; Tissera et al. 2013, 2014).

To date, only the resolved stars of the Milky Way (MW) and M31 haloes have been extensively studied. Stellar populations variations within each halo have been detected by observations in our own MW (e.g. Ivezić et al. 2008; Bell et al. 2010) as well as in M31 (Brown et al. 2006; McConnachie et al. 2009; Sarajedini et al. 2012; Gilbert et al. 2014; Ibata et al. 2014). In addition, whereas the halo of M31 has a clear negative metallicity gradient, with a change of roughly a dex in metallicity from 9 to 100 kpc (Gilbert et al. 2014; Ibata et al. 2014), there is little to no metallicity gradient in the MW, measured using stars 10–50 kpc from the centre of the MW (Sesar, Jurić & Ivezić 2011; Xue et al. 2015).[1] The order of magnitude difference in stellar halo mass (Bell et al. 2008; Ibata et al. 2014) and factor of 5 difference in metallicity and difference in gradient betray large differences in halo growth history (e.g. Gilbert et al. 2012, 2014; Deason et al. 2013). Given the stochasticity involved in the process of galaxy formation, it is important to enlarge the sample of observed galactic haloes to understand both the range of possible halo properties and what a 'typical' halo looks like.

Cosmological models of galaxy formation predict that there should be large variations among the properties of individual haloes in disc galaxies with similar mass (e.g. Bullock & Johnston 2005; Cooper et al. 2010; Tissera et al. 2014, see also earlier efforts using semicosmological simulations by Renda et al. 2005a,b.). Predictions such as differences in metallicity profiles, fraction of stellar halo created *in situ* and accreted, stellar halo morphology, etc., need to be compared against observations to differentiate between the models and quantify the predicted halo-to-halo scatter. Mouhcine et al. (2005a,b,c) presented the first study of stellar halo populations in disc galaxies outside the Local Group. Their sample consists of four massive and four low-mass disc galaxies. They resolved red giant branch (RGB) stars using the Wide Field Planetary Camera 2 (WFC2) camera onboard the *Hubble Space Telescope* (*HST*) in fields at projected galactocentric distances between 2 and 13 kpc. They found that the metallicities of the four massive MW-like galaxies are nearly 1 dex higher than the metallicity of the MW halo at a similar galactocentric distance, suggesting that massive disc galaxies with metal-poor haloes are unusual. They also found that the mean colour of the halo RGB stars in bright galaxies are redder than those in low-luminous galaxies. However, they observed one field per galaxy and thus they were not able to construct stellar population profiles as a function of radius. Moreover, given the abundant substructure present in stellar haloes, it is important to observe more than one field per galaxy at and in different directions to avoid biasing our view of the stellar halo as much as possible. Finally, the Mouhcine et al. (2005a) fields were quite close to the disc of the galaxies and were possibly subject to contamination by disc stars.

Accordingly, a number of groups have attempted to resolve the stellar populations of nearby galaxies using wide-field imagers on large ground-based telescopes. Current efforts have resolved the top magnitude or so of the RGB, and have permitted characterization of halo profile shapes, masses, axis ratios, and some characterization of stellar population properties out to galactocentric distances of ∼30 kpc (see e.g. Barker et al. 2009 and Mouhcine & Ibata 2009 for NGC 3031, Mouhcine, Ibata & Rejkuba 2010 for NGC 0891, Bailin et al. 2011 and Greggio et al. 2014 for NGC 0253). However, the precision of measurements of stellar halo RGB colour, and thus metallicity, from the ground is low, at least in part because of crowding and unresolved background galaxy contamination (Bailin et al. 2011). Moreover, ground-based measurements have not extended to more than ∼30 kpc, and in particular are not sensitive to stellar population gradients.

The Galaxy Halos, Outer disks, Substructure, Thick disks, and Star clusters (GHOSTS) survey (Radburn-Smith et al. 2011) is an extensive *HST* programme dedicated to resolve the stars in the outskirts of 16 nearby disc galaxies observing various fields along the minor and major axis of each galaxy. It is the largest study of resolved stellar populations in the outer disc and halo of disc galaxies to date. Using the RGB stars as tracers of the stellar halo population, we are able to study the size and shape of each stellar halo as well as the properties of their stellar populations such as age and metallicity. In Monachesi et al. (2013), we used the median colours of RGB stars as a function of projected radius to construct the colour profile of the stellar halo of M81 using *HST*/ACS observations from GHOSTS. We found that the colour profile of M81's stellar halo is rather flat, indicating little population gradient, out to galactocentric projected distances of ∼50 kpc. When comparing our results with model predictions for the colours of stellar haloes using simulations of stellar haloes built purely from accretion events (Bullock & Johnston 2005), we found a good agreement with the observations. Because the colour of the RGB is an approximate indicator of metallicity, this result likely reflects a flat metallicity gradient in M81's halo, which suggests a stellar halo assembly dominated by several satellites of comparable mass (Cooper et al. 2010) which were likely accreted at early times (Font et al. 2006b).

In this paper, we extend the work done in Monachesi et al. (2013) and investigate the stellar halo colour profiles of six MW-mass disc galaxies in GHOSTS, increasing the number of galaxies from which

[1] Claims of a steep metallicity gradient by Carollo et al. (2007, 2010) have since been shown to suffer from strong selection bias by Schönrich, Asplund & Casagrande (2011). Low-metallicity stars selected for study by Sloan Extension for Galactic Understanding and Exploration (SEGUE) are substantially brighter than their somewhat higher metallicity counterparts, imposing an apparent metallicity gradient.

Table 1. Properties of the six most massive disc galaxies from the GHOSTS survey.

Name NGC	α_{2000}	δ_{2000}	b	i	$V_{\rm rot}^{\rm max}$	A_V	M_B	Morph. type	DM	Mag limit adopted	Fields not used
	(h m s)	(° ′ ″)	(°)	(°)	(km s^{-1})	(mag)	(mag)		(mag)	(mag)	
(1)	(2)	(3)	(4)	(5)	(6)	(7)	(8)	(9)	(10)	(11)	(12)
0253	00 47 33.12	−25 17 17.6	−87.96	79	194	0.05	−21.23	SAB(s)c	27.7	25.6	F1, F2, F3
0891	02 22 33.41	+42 20 56.9	−17.41	90	212	0.16	−20.10	SA(s)b	29.8	26.3	F3, F9
3031	09 55 33.17	+69 03 55.1	+40.90	68	224	0.19	−20.71	SA(s)ab	27.8	25.5	F1
4565	12 36 20.78	+25 59 15.6	+86.44	90	245	0.04	−20.28	SA(s)b	30.4	27.0	F4
4945	13 05 27.31	−49 28 04.3	+13.34	85	167	0.44	−20.58	SB(s)cd	27.8	25.1	F12
7814	00 03 14.89	+16 08 43.5	−45.17	71	231	0.11	−20.15	SA(s)ab	30.8	27.2	F7

Notes. (1) NGC identifier; (2) and (3) right ascension and declination; (4) Galactic latitude in degrees; (5) inclination angle of the galaxy, as listed in Huchtmeier & Richter (1989); (6) maximum rotational velocity in km s^{-1}, as listed in Hyperleda (Makarov et al. 2014, http://leda.univ-lyon1.fr/); (7) mean V-band Galactic extinction from Schlegel, Finkbeiner & Davis (1998), Schlafly & Finkbeiner (2011); (8) total B-band absolute magnitude, as listed in Hyperleda; (9) morphological type, as listed in the NASA/IPAC Extragalactic Database (http://nedwww.ipac.caltech.edu); (10) adopted distance modulus from TRGB distance measurements obtained in Section C; (11) faintest $F814W$-band magnitude adopted in the selection box of RGB stars used for this work's analysis to assure that all the selected stars are above the 50 or 70 per cent photometric completeness; (12) fields excluded from our analysis due to severe incompleteness and/or Galactic foreground/background contamination.

we have halo stellar population gradients information by a further five galaxies. These are all nearby spiral galaxies of similar morphology, total luminosities, and stellar masses of the MW and M31. We use *HST*/ACS and Wide Field Camera 3 (WFC3) observations (a subset of which was presented by Radburn-Smith et al. 2011) to measure the median colours of RGB stars in the halo of these galaxies out to ∼70 kpc. We find a great diversity in the colour profiles of the stellar haloes of massive disc galaxies, which we interpret as reflecting differences in their metallicity profiles. The outline of the paper is as follows. In Section 2, we describe the observations and the sample of galaxies. We then explain the data reduction and photometry in Section 3. Our resulting colour–magnitude diagrams (CMDs) are discussed in Section 4. The main results of the paper are shown in Section 5 where we construct the colour distribution functions for each field/galaxy, the galaxy colour profiles, and the stellar halo colour profiles, derived using only the minor axis fields. In Section 6, we discuss our results and compare them with both observations and models. We conclude with a summary in Section 7.

2 OBSERVATIONS

We use observations from the GHOSTS survey (PI: R. de Jong).[2] GHOSTS is an extensive *HST* programme designed to resolve the individual stars in the outer disks and haloes of spiral galaxies. A detailed description of the survey can be found in Radburn-Smith et al. (2011, hereafter R-S11). Briefly, the GHOSTS sample consists of 16 nearby large angular size disc galaxies, of a range of masses ($75 < V_{\rm max}$(km s^{-1}) < 250) and inclinations (mostly edge-on) that were sampled along their principal axes. The targeted galaxies are imaged with the Advanced Camera for Surveys (ACS) and WFC3 onboard *HST* in the $F606W$ and $F814W$ filters, and their individual stars are resolved. GHOSTS observations provide star counts and CMDs typically 2–3 mag below the tip of the RGB (TRGB). The resolved RGB stars can reach very low equivalent surface brightnesses, which varies from system to system, of $\mu_V \sim 34$ mag arcsec^{-2} (Harmsen et al., in preparation). These measurements are only limited by foreground and background contamination (see Section 3.1). In order to achieve these depths, we have observed each *HST* pointing with one to eight orbits depending on the distance of the galaxy.

[2] http://vo.aip.de/ghosts/

The data were taken as part of four different GHOSTS programmes (10523, 10889, 11613, and 12213) and were complemented with archival data fulfilling the requisites discussed above.[3] The GHOSTS survey is the largest study of resolved stellar populations in the outer regions of disc galaxies to date. Such data allow us to shed light on various issues. For instance, we can use the RGB stars as tracers of the faint underlying population to obtain information about the galactic stellar haloes, such as their metallicities, stellar surface density along the minor axis profiles, and shapes (de Jong 2008; Monachesi et al. 2013, Harmsen et al., in preparation). In addition, the GHOSTS observations can be used to dissect the disks into populations of different ages and study structures of stellar populations separately (de Jong et al. 2007; Radburn-Smith et al. 2014; Streich et al. 2016) as well as to discover faint dwarf galaxies (Monachesi et al. 2014).

2.1 Galaxies studied in this work

In this paper, we focus on the six most massive galaxies of the GHOSTS sample, which have maximum rotation velocity $V_{\rm max} \gtrsim 170$ km s^{-1}. These are all spiral galaxies of similar morphology, total luminosities, and stellar masses of the MW and M31. Table 1 summarizes the main properties of the six galaxies studied in this paper. Four of these galaxies are edge-on and two are highly inclined. Thus, they are ideal for stellar halo studies since one expects little disc contamination when they are observed out to large radii along their minor axis. For each of these galaxies, we have several *HST* pointings spaced along the minor and major axes. We have also observed fields in regions that are half-way between the major and minor axes, which are called intermediate axis fields throughout the text for simplicity. This strategy allows us to probe the stellar haloes out to large projected distances from the galactic centre. We typically have fields observed out to $R \sim 50$ to 70 kpc along the minor axis.

Figs 1 to 6 show colour images of the six GHOSTS galaxies studied in this work with the ACS/WFC and WFC3/UVIS fields overlaid. Fields in green represent the ACS/WFC data presented in

[3] These *HST* programmes have contributed to GHOSTS observations: 9353, 9414, 9765, 9864, 10136, 10182, 10235, 10584, 10608, 10889, 10915, 12196, 13357, 13366.

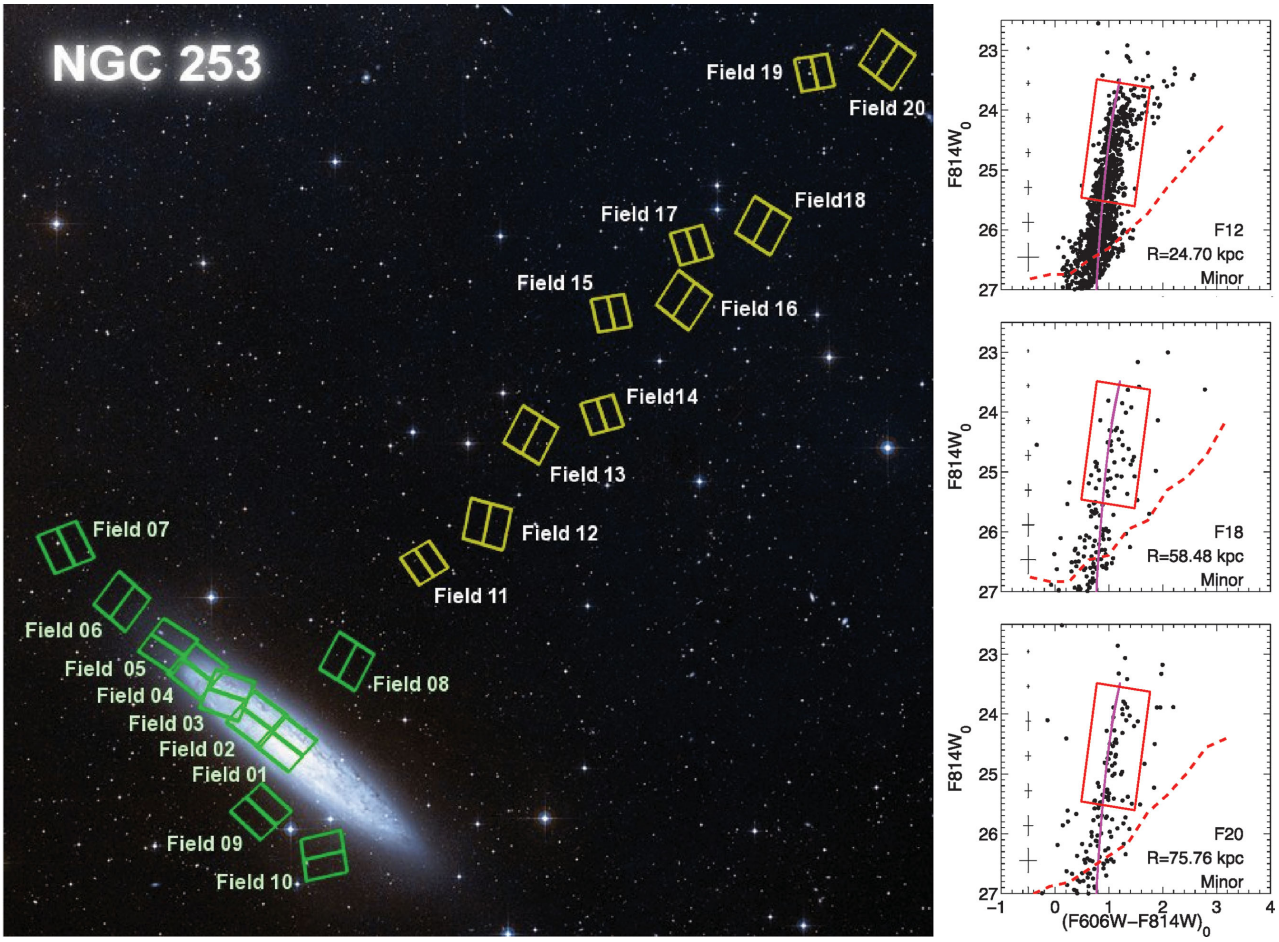

Figure 1. Left-hand panel: DSS coloured image of NGC 0253, showing the location of the *HST* ACS/WFC and WFC3/UVIS fields. North is up and east is to the left. ACS fields in green were already introduced in R-S11 whereas ACS and WFC3 fields indicated in yellow are new observations. Right-hand panel: three CMDs of fields at different distances from the centre of the galaxy, indicated in each panel in kpc, with increasing distance from top to bottom. Only the stars that remain after the masks and the culling were applied to the DOLPHOT photometry output. Magnitudes are calibrated on to the VEGAmag *HST* system and corrected for Galactic extinction (see Table 1). Label 'Minor' ('Major') indicates that the field is located on the minor (major) axis of the galaxy. The stars inside the red box are above ∼50 per cent or 70 per cent completeness (depending on the galaxy) and were used to compute the colour distribution functions and determine the colour and width profiles in Figs 9–14. A 10 Gyr old isochrone with [Fe/H] = −1.2 dex from BaSTi stellar evolutionary models (Pietrinferni et al. 2004) is superimposed in each CMD to provide the reader with an idea of the old stellar populations present in these fields. RGB stars redder and bluer than the isochrone we assume indicate more metal-rich and more metal-poor stars than [Fe/H] = −1.2 dex. The red-dotted line indicates the 50 per cent completeness level and the errorbars are the photometric errors as a function of magnitude at colour = 1, as derived from the artificial star test results. We show CMDs from new observations, the CMDs of all the fields in green are presented in R-S11 and all the CMDs are presented on the GHOSTS website (http://vo.aip.de/ghosts/).

R-S11 whereas yellow fields are new ACS/WFC and WFC3/UVIS observations. For most of the galaxies, we observed fields along both the minor and major axes, which allows us to place constraints on the stellar halo shapes or axis ratios (Harmsen et al., in preparation). For some galaxies, such as NGC 0253, fields along the minor axis were prioritized. Information about each individual field is provided in Appendix A.

3 DATA REDUCTION AND PHOTOMETRY

The data reduction steps and photometry were performed using the GHOSTS pipeline described in R-S11 for the ACS data. We briefly summarize the general procedure and refer the reader to the R-S11 paper for full details. There are however some differences with respect to the data processing presented in R-S11 which we highlight and describe below. In particular, we describe here the differences in the treatment of the WFC3/UVIS data, which was not presented in R-S11. We note that we have rerun the new GHOSTS pipeline on all our data, both those presented in R-S11 and the new data introduced here.

We downloaded the images from the Hubble Data Archive MAST (Mikulski Archive for Space Telescopes). The ACS/WFC data can be directly obtained as `*_flc` FITS images, which have been passed through the new version of CALACS package containing a pixel-based charge transfer efficiency (CTE) correction (Anderson & Bedin 2010). The FLC images have been bias-subtracted, then passed through a basic cosmic ray rejection step, have been flat-fielded, and finally corrected for CTE. For the WFC3/UVIS images, however, we have generated the FLC images locally since the pixel-based CTE correction is not yet a part of the WFC3/UVIS pipeline. We have run a code, provided by STScI, on the `*_raw` FITS images to generate the corresponding FLC images. The WFC3/UVIS code uses a very similar algorithm to the one that is currently a part of the ACS/WFC pipeline.

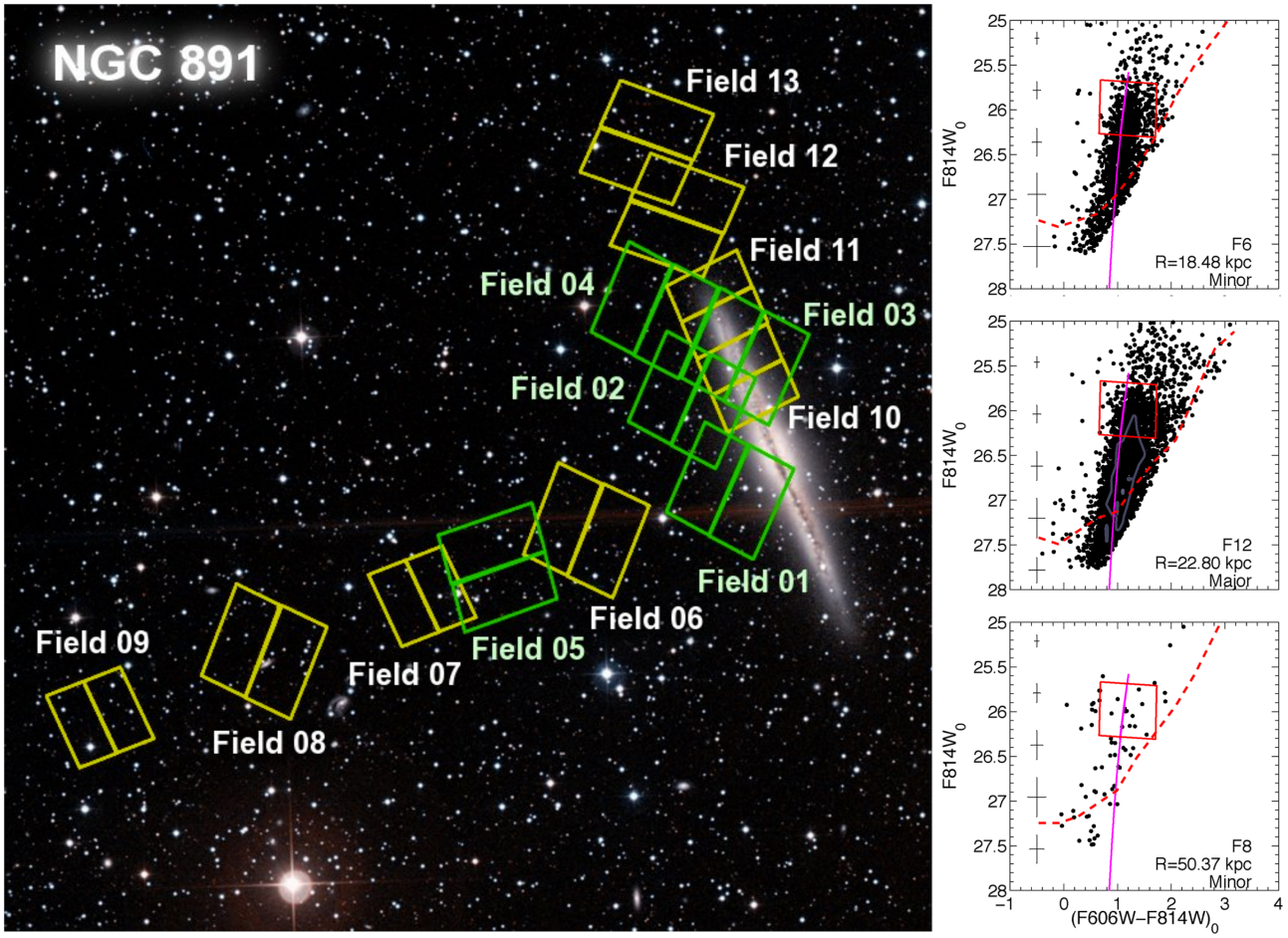

Figure 2. Same as Fig. 1 for NGC 0891. Due to the low latitude of this galaxy, these fields are contaminated by more MW foreground stars than a typical GHOSTS field. In particular, foreground white dwarf stars may contaminate the region inside the red box from which we select the stars for further analysis. In order to clean these fields from MW stars, we have used Field 9 as a control field and decontaminated statistically each other field from its stars. We do not use Field 9 in our analysis, although a handful of its stars (fewer than eight) may actually belong to NGC 0891. The CMDs shown here have not been yet cleaned using Field 9. See Section 4 for details and Fig. 7 for example decontaminated CMDs. The decontamination mainly affects Field 8.

We have combined the individual FLC images using the ASTRODRIZZLE package (Gonzaga 2012), which aligns the images, identifies any additional cosmic rays, removes distortion, and then combines the images after subtracting the identified cosmic rays. The output of running ASTRODRIZZLE on FLC images are DRC FITS images, which we use as a reference frame for coordinate positions; we do not perform photometry on them.

Stellar photometry was performed using the ACS and WFC3 modules of DOLPHOT, a modified version of HSTPHOT (Dolphin 2000). DOLPHOT performs point spread function (PSF) fitting on all the flat-fielded and CTE-corrected images (FLC) per field simultaneously. A refinement of the shifts between the World Coordinate System (WCS) of the observations, scale, and rotation adjustments is done by DOLPHOT after a first estimate of these tasks is done by ASTRODRIZZLE. We have used the synthetic Tiny Tim PSFs (Krist 1995; Hook, Stoehr & Krist 2008; Krist, Hook & Stoehr 2011) for the ACS images and the Jay Anderson PSFs (ISR ACS 2006-01) for the WFC3 images, to centre and measure the magnitude of each star in both filters. We note that the Tiny Tim PSFs were initially used for the WFC3 images as well. However, the systematics between the magnitudes of coincident stars in overlapping regions, which are most likely due to a combination of PSF and CTE uncertainties, were worse, with offsets up to 0.1 mag at the bright end. When the Anderson PSFs were used on the WFC3 images, the photometric measurements showed smaller systematic offsets, indicating that the Anderson PSFs were closer match to the real PSF profiles (see Williams et al. 2014, for a discussion on systematics due to PSF). The DOLPHOT parameters used on the GHOSTS fields are similar to those used in the Panchromatic Hubble Andromeda Treasury (PHAT) programme (Dalcanton et al. 2012) and are indicated in Table A2 in Appendix A. The final output of DOLPHOT provides instrumental VEGA magnitudes, already corrected for CTE loss and with aperture corrections calculated using isolated stars. The photometric output also includes various diagnostic parameters that are used to discriminate detections such as cosmic rays and background galaxies from actual stars (see Section 3.1 and Appendix B).

An additional step was performed on some of the WFC3 fields that had one single exposure in the *F*606*W* band.[4] Because some cosmic rays can appear indistinguishable from stars, without a second exposure the automatic pipeline described previously cannot remove them in these single exposure *F*606*W* images. Subsequently,

[4] The WFC3 fields that have one single exposure in the *F*606*W* band are: Fields 13, 15, 18, 19, 21, 23, 25, and 27 in NGC 3031; Field 14 in NGC 0253; Fields 2, 4, 6, 7, 9, and 11 in NGC 4945.

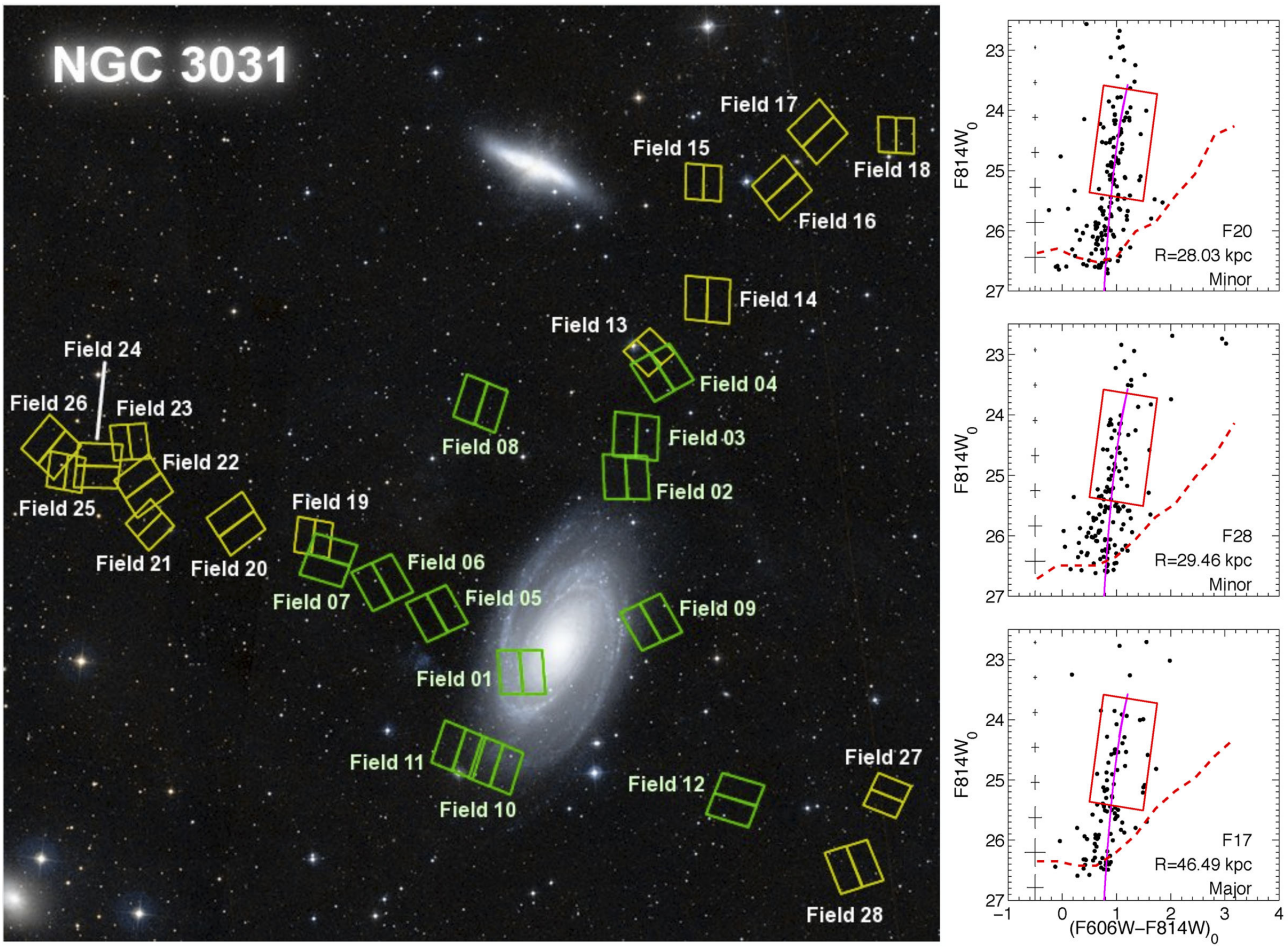

Figure 3. Same as Fig. 1 for NGC 3031.

DOLPHOT chose these bright, point-like cosmic rays as ideal 'stars' from which to determine aperture corrections. As a consequence, the aperture corrections for those fields, and thus the apparent magnitudes, were systematically off. To fix this, we have used the detected CMD locations of cosmic rays in the raw DOLPHOT output. As the cosmic rays appear in a CMD as bright $F606W$ detections with very faint $F814W$ sources (likely hot pixels), we have selected the compact sources which are implausibly blue in $F606W$–$F814W$; all other point sources in a CMD are likely to be bona fide stars. We then masked the cosmic rays out in the original $F606W$ FLC image and re-run DOLPHOT again on those fields.

3.1 Contaminants

The most important source of contamination in the GHOSTS images are unresolved background galaxies. We have estimated the background galaxy density using the GALAXYCOUNT program (Ellis & Bland-Hawthorn 2007). Since the depth of our data varies significantly from galaxy to galaxy, mainly due to their different distances, the number of background galaxies will also vary. For the images of the nearer galaxies, with 50 per cent completeness at $F814W \approx 26$ mag, the number of unresolved galaxies per arcmin^{-2} is 21, 50, 92, and 132 at $F814W < 24$, <25, <26, and <27 mag, respectively. For the more distant galaxies, with 50 per cent completeness at $F814W \approx 28$ mag, the number of unresolved galaxies is 55, 120, 228, and 366 arcmin^{-2} at $F814W < 25$, <26, <27, and <28 mag, respectively. The number of unresolved background galaxies is significant, particularly when one wants to analyse the outermost fields which may contain only hundreds of real stars. Several selection criteria, i.e. culls, to discriminate unresolved galaxies from stars were optimized using 'empty' deep archival high-redshift *HST*/ACS and *HST*/WFC3 fields. These 'culls' were applied to the corresponding raw photometric outputs from ACS and WFC3, which removed ∼95 per cent of the DOLPHOT detections in the high-redshift 'empty' fields. Details on the photometric culls and how they were optimized for the WFC3 data can be found in Appendix B. The optimization for the ACS culls[5] can be found in R-S11.

Contamination from Galactic foreground stars was estimated using the TRILEGAL model (Girardi et al. 2005, http://stev.oapd.inaf.it/cgi-bin/trilegal), for the magnitude range $F814W = 22$–28 and colours $(F606W - F814W) > 0$. We find that within those ranges, less than 25 and 18 foreground stars are expected per ACS and WFC3 field, respectively, with the exception of NGC 4945 and NGC 0891, which are at a low Galactic latitude, and thus their fields are more contaminated from MW stars within the same magnitude and colour ranges (770 MW stars in NGC 4945 fields and 97 stars in NGC 0891; see Section 4). The foreground contamination was also estimated using the Besançon Galaxy model (Robin et al. 2003, http://model.obs-besancon.fr/); however, this model predicted between 0 and 4 stars per ACS field

[5] We have applied the sparse-field culls to all our ACS fields.

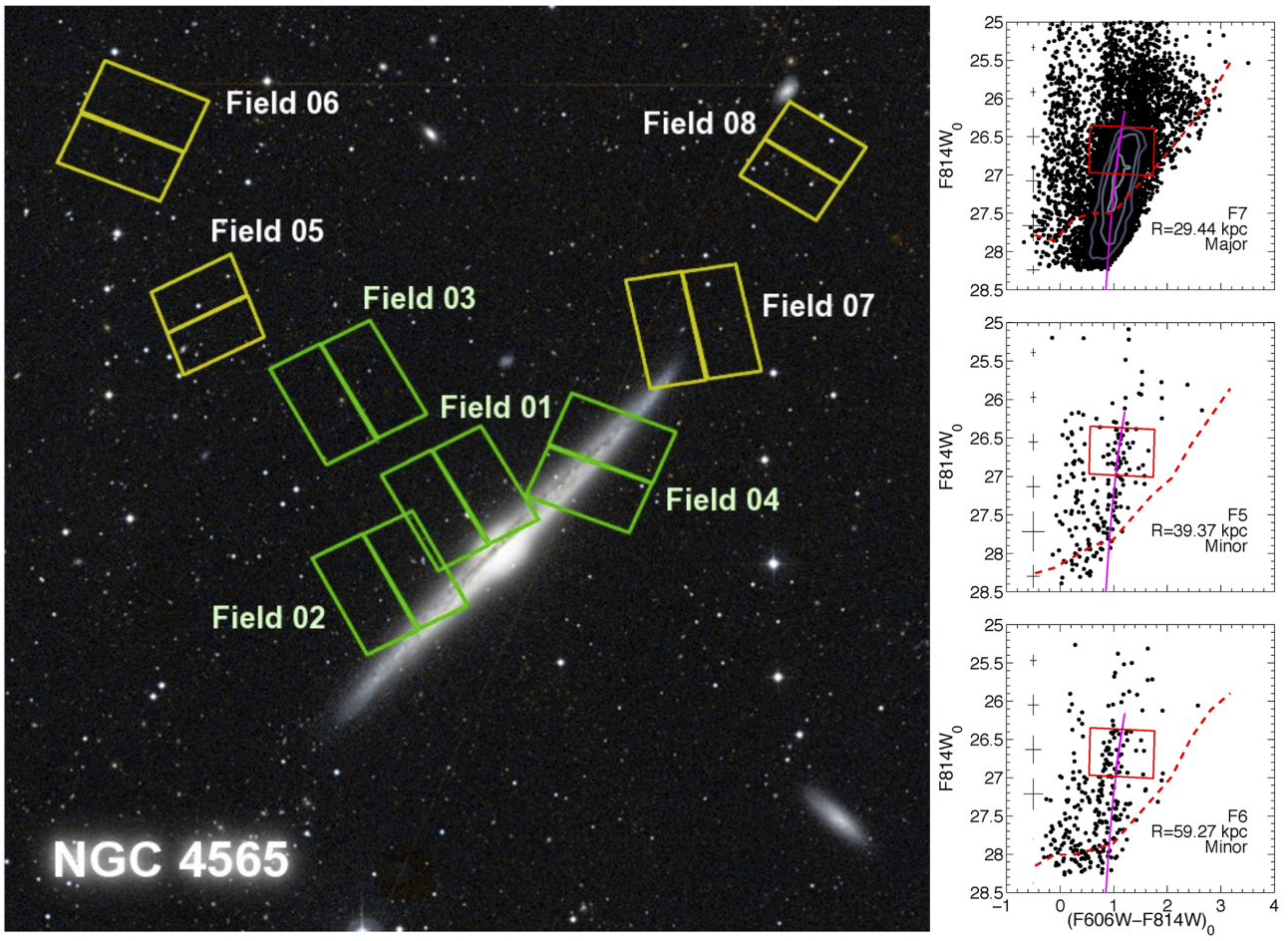

Figure 4. Same as Fig. 1 for NGC 4565. We note that Field 6 has an spatial overdensity of stars which is likely a halo substructure, either a stellar stream or a satellite dwarf galaxy. It is noticeable in the CMD as a bluer RGB, parallel to the isochrone superimposed. Further investigation is needed to understand the origins of the detected overdensity which is out of the scope of this paper. We emphasize, though, the power of *HST* in resolving halo substructures, despite the small FoV (see also Monachesi et al. 2014). We also note that the bluer detections, with colours between −0.2 and 0.5, that are seen in the outer Fields 5 and 6 are in part background galaxies/quasars that passed the culls, as we can see in Fig. B1 in Appendix B. However, some of them may be young stars which may associated with the detected overdensity of stars in Field 6.

within the magnitude and colour ranges chosen, which is clearly an underestimation as they can be observed in larger numbers in the CMDs of the GHOSTS galaxies (Figs 1 to 6).

In addition, a mask of all extended and resolved objects was constructed for each field using SExtractor (Bertin & Arnouts 1996). Detections lying in the pixel positions of the masked sources were discarded from the star catalogue. An extra step was carried out for the fields in the crowded disc regions, since the resulting mask from SExtractor had essentially masked out the entire disc. We unmasked everything that was not obviously a background galaxy or bright foreground star in order to get detections in the disc and any cluster.

3.2 Artificial star tests

Extensive artificial star tests (ASTs) were performed to assess the completeness level and quantify the photometric errors of the data. The procedure of the ASTs are explained in detailed in R-S11. In short, approximately 2000000 artificial stars per field are injected and photometred by dolphot, one at a time to avoid affecting the image crowding. The artificial stars were distributed according to the observed stellar gradient, thus the higher surface brightness regions of an observation were populated with more artificial stars. The colours and magnitudes of the injected artificial stars are realistic and they cover not only the observed values but also fainter magnitudes to explore the possibility of recovering faint stars and assess their contaminating effect on observed stars. We applied the same culls as in the real images. Artificial stars that did not pass the culls were considered as lost. The completeness level was calculated as the ratio of recovered-to-injected number of artificial stars at a given colour and magnitude bin.

4 COLOUR–MAGNITUDE DIAGRAMS

The bottom panels of Figs 1 to 6 show the CMDs of some representative fields in each galaxy that were not previously presented in R-S11, at different galactocentric projected distances and along the galaxy's minor and major axes. All of the CMDs are shown in the GHOSTS website for the interested readers.[6] The CMDs were generated after the masks and culls were applied, thus we expect little contamination from background-unresolved galaxies in them.

[6] http://vo.aip.de/ghosts/

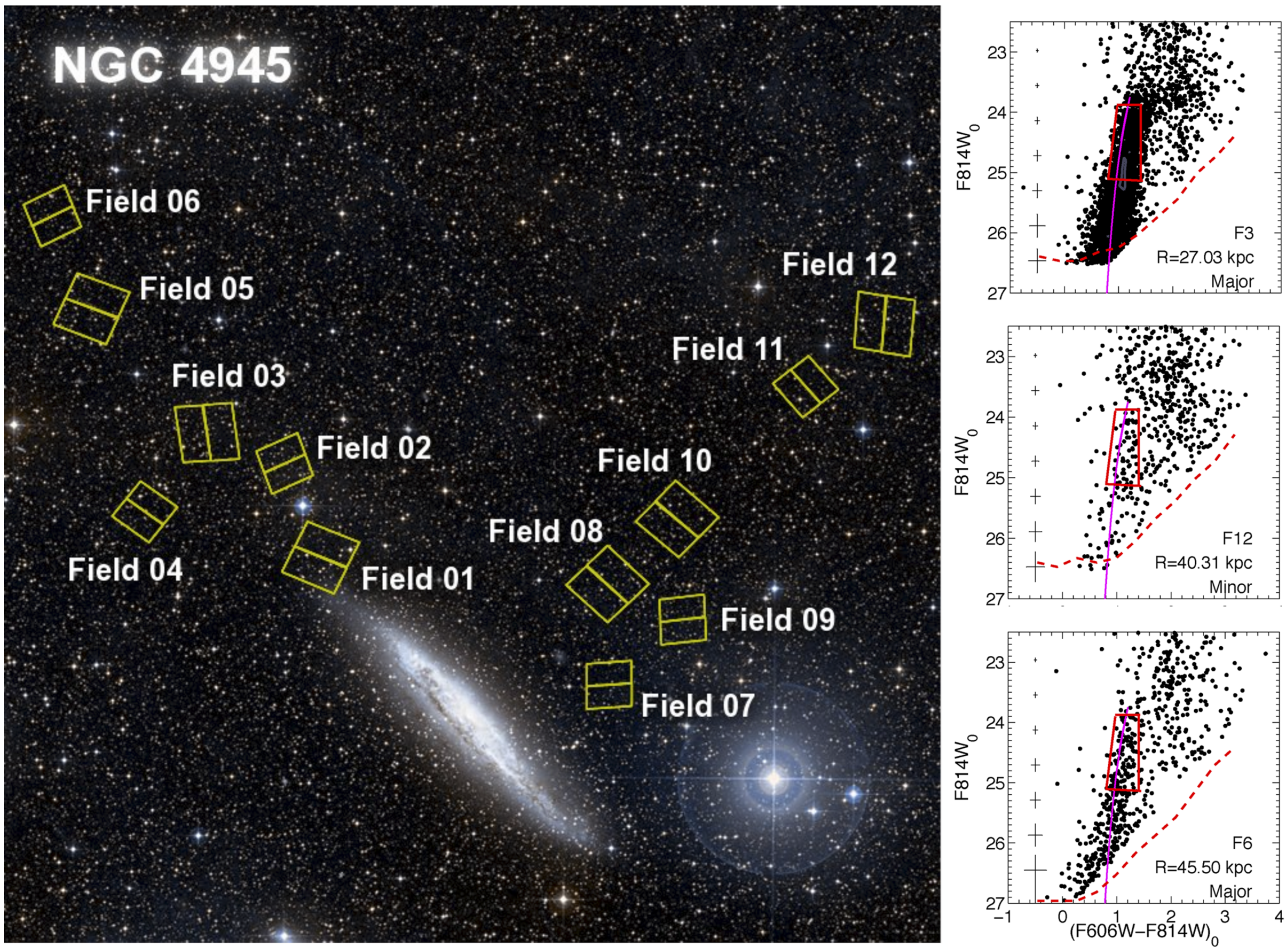

Figure 5. Same as Fig. 1 for NGC 4945. Note that the MW foreground, stars brighter than $F814W \sim 24$ as well as at colours redder than ∼1.4, is substantially higher than for the other galaxies owing to its low Galactic latitude. The red box used to select the stars for this work's analysis has a colour cut at 1.4; the region bluer than that at the magnitude range selected should have the least contamination from foreground stars. We expect Field 12 to be partly or completely dominated by foreground MW stars and we therefore discard this field in our analysis.

The magnitudes have been corrected for Galactic extinction using the corrected extinction ratios presented by Schlafly & Finkbeiner (2011) that are to be used with the $E(B-V)$ values from the Schlegel et al. (1998) dust maps. The 50 per cent completeness level of each field as well as their projected radial distance from the galaxy centre are indicated in each CMD. We note that, as we do not know the axis ratio of the stellar haloes and the galaxies are mostly edge-on, we calculated the projected distances using circular symmetry.

As already mentioned, the depth of the GHOSTS CMDs, and thus their 50 per cent completeness level, varies from galaxy to galaxy depending mainly on their distance. Within fields of the same galaxy, there may also be differences in depth since fields closer to or on top of the galactic disc are limited by crowding and are therefore shallower than those further out. Typically, the 50 per cent completeness level is found at one to two magnitudes below the TRGB, indicated as the upper magnitude limit of the red box superimposed in each of the CMDs in Figs 1 to 6. Since the absolute I magnitude of the TRGB is almost constant ($M_I \sim -4.05$) for populations older than 3 Gyr and metallicities lower than [Fe/H] ~ -0.7 (Bellazzini, Ferraro & Pancino 2001), this evolutionary feature can be used to determine the distance to a galaxy. The TRGB magnitudes and thus the distances for most of the GHOSTS galaxies were already measured by R-S11. We measured in this work the TRGB distances of the new data which can be found in Appendix C. A complete list of all of the GHOSTS TRGB distances is also provided in Appendix C.

The CMDs are mostly populated by old RGB stars (older than 1 Gyr). There are however younger populations such as blue, extended main-sequence (MS) stars (< 500 Myr) or massive stars burning helium in their core (25–600 Myr old red and blue loop sequence stars). These appear primarily in the fields closer than $R \sim 15$ kpc to each galaxy, and especially along the major axis, which are dominated by disc stars.

As we noted in Section 3.1, contamination from foreground MW stars is generally very little in our fields, as modelled by TRILEGAL code. For NGC 4945, however, this contamination is significantly higher than the other galaxies owing to its low latitude. In addition, there is a noticeable difference in the amount of foreground stars from field to field since the region surveyed around NGC 4945 covered ∼0.°5 × 0.°5 on the sky. We compared the CMDs and colour distributions of fields simulated by TRILEGAL at the different Galactic coordinates of our 12 GHOSTS fields. The corresponding photometric errors on each field as obtained from the ASTs were applied to the models in order to make a fair and quantitative model-observation comparison (see Monachesi et al. 2012, 2013 for details on how the observational effects are simulated in the models). We find that while the number of foreground stars appears to reasonably agree with the observations, based mostly on Fields 11

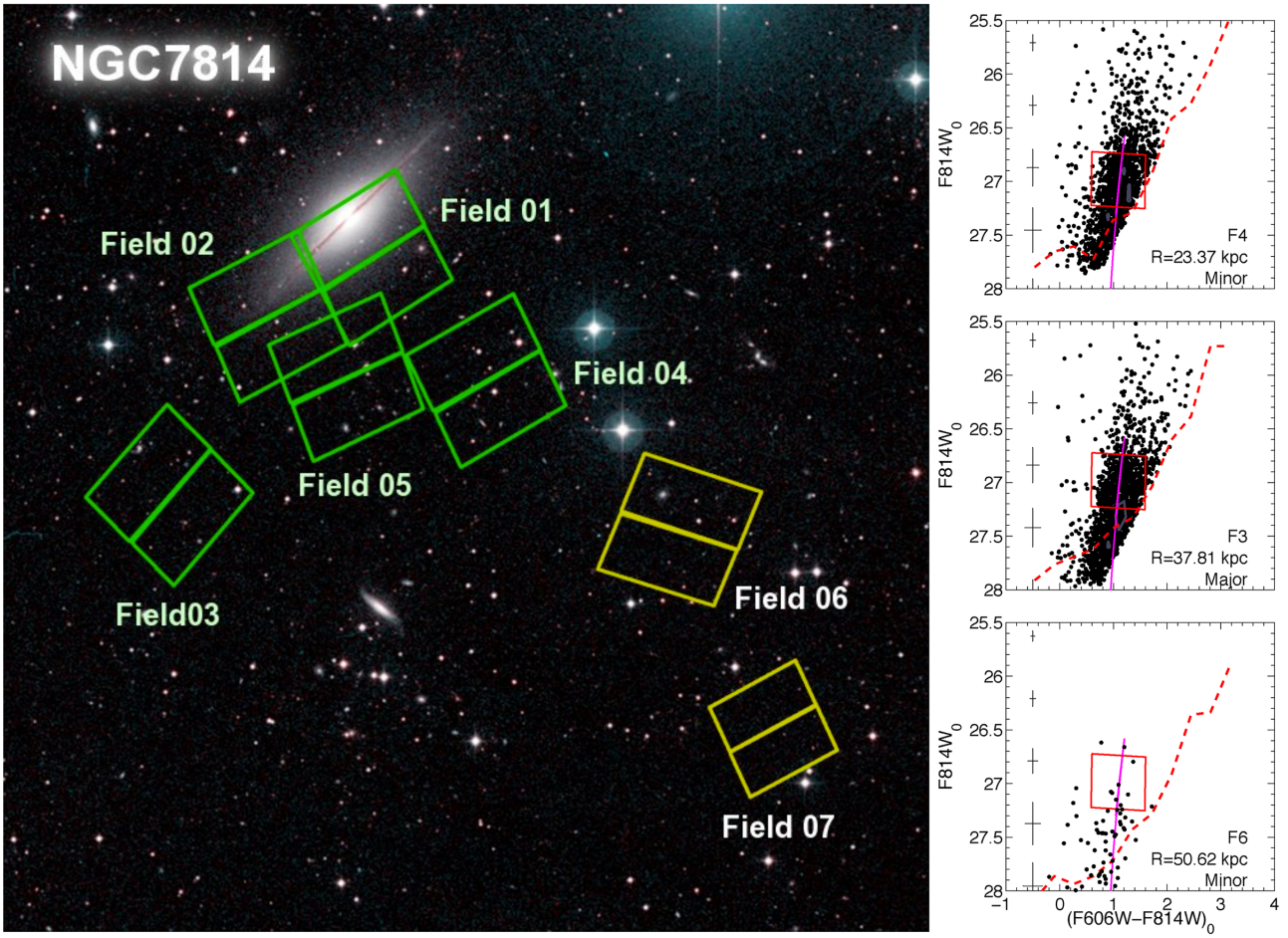

Figure 6. Same as Fig. 1 for NGC 7814. Note that the limiting depth in the *F*606*W* filter as well as the choice of the selection box truncates the colour range considered for this galaxy. We discuss this further in Section 5.1. We note, as in NGC 4565, that there are few bluer detections, with colours between −0.2 and 0.5. These are most likely background galaxies/quasars that passed the culls, as we can see in Fig. B1 in Appendix B.

and 12 which are the sparser and thus the fields with a higher fraction of contaminants, the TRILEGAL colours are bluer by ∼0.75 mag. When we shift the colours to match the observations, we find that the MW contribution is negligible for colours bluer than ∼1.4 and at magnitudes fainter than the TRGB. We thus decide to make a colour cut of 1.4 and we do not consider redder stars when analysing these fields. Brighter MW stars may appear bluer but we do not use that region of the CMD for our analysis (see red box in Fig. 5 used to select the RGB stars for computing the colour profiles). Finally, inspecting how the foreground MW stars should look as simulated by TRILEGAL code and the CMDs of the NGC 4945 fields, we conclude that Field 12 is dominated by MW stars and we subsequently discard it from further analysis.

NGC 0891 is also at a low Galactic latitude and we noticed that its fields are not only contaminated by bright foreground stars, which occupy a CMD region that does not overlap with the RGB at the distance of NGC 0891, but also by white dwarf MW stars, likely from the Monoceros Ring (Slater et al. 2014). This foreground contamination, at $F814W \sim 26$–27 and colours between 0 and 1 (Calamida et al. 2014) is not an issue for the majority of the fields which are well populated, but it becomes significant for Fields 8 and 9, which are very sparse. We believe that the stars in the selected RGB region used to measure the median colour (see the next section) in Field 9 are mostly contaminants, from both MW stars and some background galaxies that passed the culls. We therefore consider Field 9 as a control field and statistically decontaminate the rest of the NGC 0891 fields from its detections as follows. For each star in Field 9 that is fainter than $F814W = 25.4$, we removed the closest star in each other field's CMD that has a magnitude and colour within 0.3 and 0.4 mag, respectively. Since Field 9 is a WFC3 field, thus it covers a smaller area on the sky than an ACS field, the number of stars subtracted in the ACS fields is corrected to take into account the differences in area. Fig. 7 shows two examples of how the CMDs appear after decontaminating for Field 9 stars as well as the CMD of Field 9. The effect is noticeable most strongly in Field 8 however the calculated colours in Field 7 are also affected by this decontamination. Because the number of stars in Field 9 is more than the typical number of remaining background galaxies within $F814W \sim 25.5$ and 27 and many more than the predicted MW white dwarf stars that should be at that Galactic latitude and longitude, few stars in Field 9 may actually belong to NGC 0891 (fewer than eight, from which only three will lie inside the selection box as we can see in Fig. 7). However, it is impossible to discern if these are actually field stars or background galaxies that passed the culls. We therefore discard Field 9 from our analysis.

It is important to emphasize that *all* of these galaxies have halo stars out to at least 50 kpc *along the minor axis*, which is more than 50 scaleheights of the MW's thick disc. Thus, our observations show

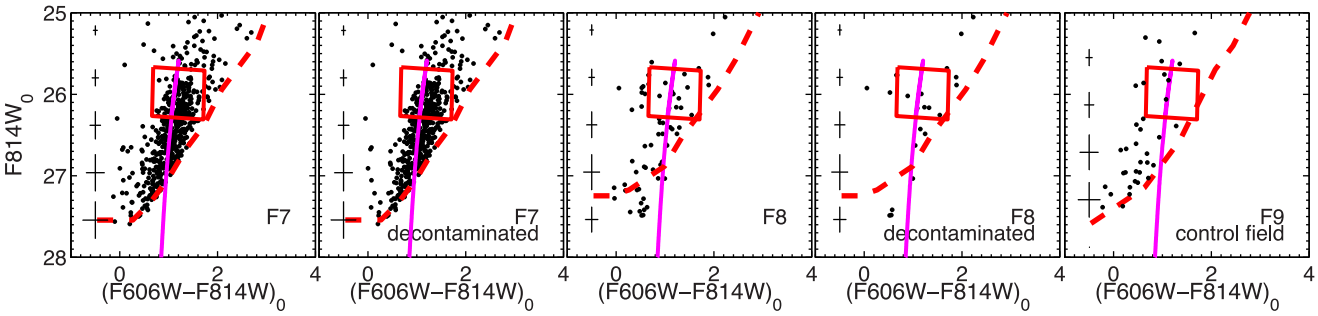

Figure 7. CMDs of two fields in NGC 0891, Field 7 (first panel) and Field 8 (third panel) and their resulting CMDs after decontamination for foreground MW white dwarf stars (second and fourth panels, respectively) as well as for some background galaxies that passed the culls. Field 9 of NGC 0891 (last panel) was used as a control field and its stars were statistically subtracted from each other field in NGC 0891. See Section 4 for details.

that the highly inclined massive disc galaxies ($V_{\rm max} \gtrapprox 170$ km s^{-1}) have clear extended stellar haloes beyond the region where the disc dominates.

5 RGB STARS AS STELLAR HALO TRACERS: THEIR COLOURS

In this section, we use the RGB stars in each galaxy to analyse their colours as a function of galactocentric distance. We analyse our data in terms of colours rather than in metallicities, which would require a colour–metallicity transformation, because age and metallicity are partially degenerate in the RGB evolutionary phase (see e.g. Worthey 1994). It is therefore impossible to constrain the ages and metallicities of the RGB stars from only the CMDs that we observe. Nevertheless, it is well known that the effects of age are relatively small compared to metallicity, such that the colour of the RGB is an approximate indicator of metallicity (Hoyle & Schwarzschild 1955; Sandage & Smith 1966). In the next section, we will assume that the colour profiles of the RGB stars reflect metallicity profiles when comparing our results with other observations and models.

5.1 Colour distribution functions

We calculate the colour distribution function per field using RGB stars within a magnitude range extending from the TRGB down to a magnitude limit for each galaxy as indicated in Table 1. We adopt a magnitude limit to ensure that stars are brighter than the 50 per cent or 70 per cent completeness level in all the fields and have small photometric errors. This limit is not the same for all galaxies because the depth of the CMDs, and thus their 50 per cent completeness level, varies from galaxy to galaxy, with nearer galaxies exhibiting deeper CMDs. The brighter magnitude limit (the TRGB) minimizes contamination from bright asymptotic giant branch (AGB) stars or other contaminants, mainly MW foreground stars. In addition, since we are interested in the properties of the RGB stars that constitute the bulk of the stellar halo populations, we select stars for study within a restricted colour range chosen by eye. The blue limit avoids contamination from blue MS/HeB young stars that appear in some fields closer to the disc, whereas the red limit avoids metal-rich disc or MW foreground stars as well as incompleteness in the case of the more distant galaxies (see e.g. the CMDs of NGC 7814) in order to assure the 50 per cent completeness level of the stars analysed. The red and blue limit slopes of the selection boxes are the same as the RGB slope of the 10 Gyr old isochrone with [Fe/H] $= -1.2$ dex plotted in each CMD in Figs 1 to 6. The selection box for each galaxy is shown as a red rectangle in Figs 1 to 6. For consistency, we use the same box for all the fields within a galaxy. Possible systematic biases that might be introduced due to the different selection boxes among the galaxies are discussed and addressed in Appendix D. We demonstrate in Appendix D that selection boxes differences have little impact on our main results presented in the next sections.

In addition to the variation in the CMD depth from galaxy to galaxy, the depth of the CMDs may vary from field to field within the same galaxy, where fields closer to or on top of the galactic disc are limited by crowding and are therefore shallower. We note that the faint magnitude limit mentioned above ensures the 50 per cent completeness level of the shallower data. However, fields with CMDs that are much shallower than the rest of the fields in the same galaxy were discarded when measuring the colour distribution and the median colour of its RGB stars. These are indicated in the last column of Table 1. Other fields that were not considered when measuring the median colour profile include Field 12 of NGC 4945, which is dominated by MW foreground stars, Field 9 of NGC 0891 whose selected region of RGB is dominated by white dwarf MW foreground stars and residual background galaxies that passed the culls, as discussed in Section 4, and Field 7 of NGC 7814 which has only three stellar detections. They are also indicated in the last column of Table 1.

In order to obtain a colour distribution that better reflects the spread in metallicity on a given observed field, we define a new colour index Q by slightly rotating the CMDs an angle of $-8\overset{\circ}{.}29$, where a line of slope -6.7 becomes vertical. The rotation is such that the magnitude axis (y-axis) of each CMD is parallel to a 10 Gyr old [Fe/H] $= -1.2$ dex isochrone[7] shown in the CMDs of Figs 1 to 6. Fig. 8 shows the normalized colour distribution functions of Field 22 of NGC 3031 in the true colour ($F606W - F814W$) in black as well as in the rotated Q-index colour in red. This exemplifies the effect of going from the true to the Q-index colour in the colour distribution functions. The CMD rotation yields a tighter colour distribution, which also better reflects the metallicity distribution.

The left-hand panels in Figs 9 and 10 show examples of the normalized Q-index colour distribution functions for three fields in each galaxy, plotted as histograms. The field numbers from which

[7] We chose this particular isochrone as it qualitatively matches reasonably well the RGB shape of the halo CMDs for NGC 3031, NGC 4565, and NGC 7814. For the other three galaxies, no single isochrone is a good match to the RGB shape, but this isochrone does match both the bluer RGB stars and captures much of the slope of the RGB even for higher metallicity isochrones.

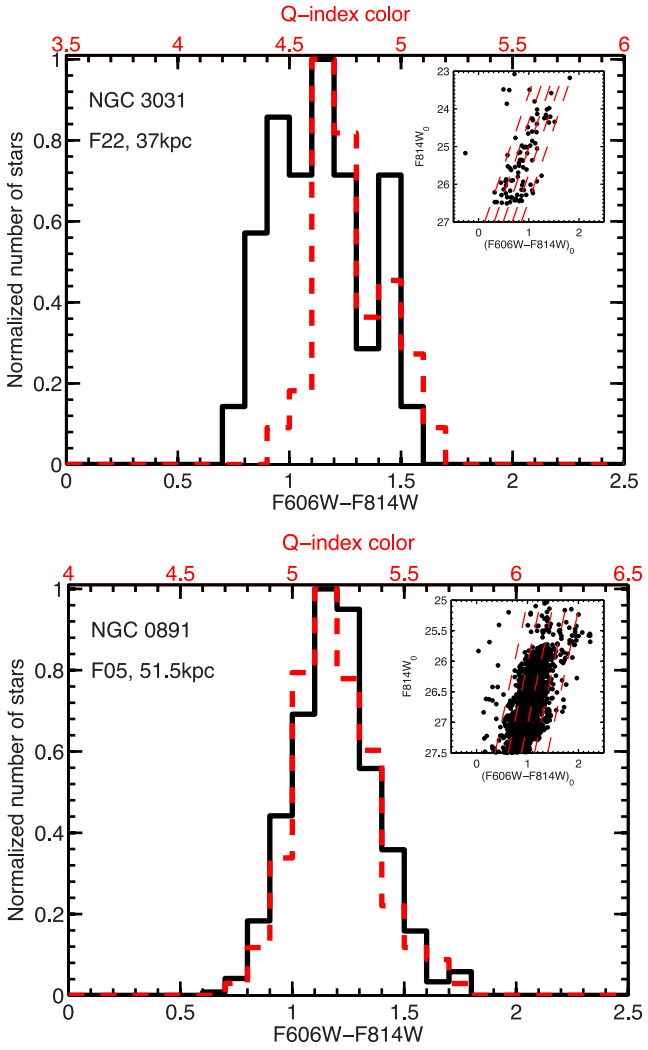

Figure 8. Colour distribution functions in ($F606W$–$F814W$) and Q-index colours, as black and red histograms, respectively, for Field 22 in NGC 3031 (top panel) and Field 5 in NGC 0891 (bottom panel). The colour distribution becomes tighter when using the Q-index colour. The Q-index colour distribution reflects the metallicity distributions better than the true colour distribution. The peak of this distribution in the bottom panel is at a redder colour than that in the top panel, reflecting a higher metallicity for the NGC 0891 field. The inset figures show the CMDs of the same fields with dashed lines indicating constant Q-index colours. The red and blue limits of the selection boxes for these galaxies are shown as the rightmost and leftmost lines on the CMDs, respectively.

the distributions are shown as well as their galactocentric distances are indicated in each panel. Some field numbers have a subscript 1; this is because the fields of the more distant galaxies have been divided in either three or four regions as explained in the next subsection. What we shown in those cases is the colour distribution of one of the regions per field.

Looking at the colour distribution functions, we find differences in both the range of colours and the dominant colour from galaxy to galaxy and in some cases from field to field within the same galaxy. This can also be appreciated in the middle and right panels of Figs 9 and 10, where we show the cumulative colour distribution function for fields closer and farther than 30 kpc, respectively. The grey-dashed line in each figure shows the cumulative colour distribution resulting from a fiducial CMD model of 10.5 Gyr and $[\mathrm{Fe/H} = -1.2 \pm 0.3]$ dex, generated using IAC-STAR code (Aparicio & Gallart 2004). The observational effects corresponding to each galaxy were simulated using the results from the ASTs (see Monachesi et al. 2012, 2013) and the same selection of RGB stars per galaxy as well as the CMD rotation to obtain the Q-index colour were applied to the model. A visual comparison between the cumulative colour distribution of the fiducial model and that of observed fields indicates where the median colour and range of colours of each field differs or agree with that of the model. We quantify the differences between the colours of each field and the range of colours observed, i.e. the width of the colour distribution functions, in the next subsections.

We note that the colour distribution functions of our most distant galaxies, NGC 7814 and some fields of NGC 891, are incomplete for red colours owing to a limited depth in $F606W$-band images (see Fig. 6). We are thus unable to observe the reddest stars in these fields. Moreover, the redder stars that we do observe have larger photometric uncertainties and the choice of the RGB selection box truncates the colour range observed to assure that all the stars analysed are above ∼60 per cent completeness level. We therefore consider that the median colours and the width of the colour distributions presented for the fields in NGC 7814 are a lower limit of the actual values.

5.2 Galaxy colour profiles

We discuss in this section the global colour profiles for the GHOSTS galaxies, using all the fields analysed in this work. We focus on the stellar halo colour profiles in the next section.

Fig. 11 displays the global median colour profile of each galaxy as a function of projected radius. Red, blue, and black dots indicate measurements obtained in fields along the major, minor, and intermediate axis, respectively. The errorbars indicate uncertainties in the median values calculated by bootstrapping our sample of RGB stars as well as systematic uncertainties due to calibration which accounts for up to ∼0.04 mag in colours (see below).

To derive the colour profiles, we obtain the median colour of the selected RGB stars at different projected galactocentric distances.[8] We first calculate the median of the Q-index colours, which we then rotate back to the original coordinates of $(F606W - F814W)$ colour using a magnitude that is 0.5 mag below the TRGB. Because we select the sample of RGB stars within different magnitude ranges on a galaxy by galaxy basis (described in the previous section), the normalization of each measurement to a colour at a same absolute magnitude makes the colour median values comparable from galaxy to galaxy.

Each median colour measurement represents the star colours in an approximately 3 kpc region on a side (approximately 10 kpc^2 area). For the three nearest galaxies (NGC 0253, NGC 3031, and NGC 4945), we obtain a median colour measurement per *HST* field. These galaxies are at a distance of ≈4 Mpc and the size of their *HST* fields extends over roughly the same linear distance, covering ≈ 3.5 and 2.8 kpc on a side of the ACS and WFC3 field of view (FoV), respectively. However, NGC 0891, NGC 4565, and NGC 7814 are at further distances, indicated in Table C1. Therefore, the FoVs of the fields located around these galaxies cover larger

[8] Fields 14 and 15 of NGC 3031 contain one massive globular cluster each (Jang et al. 2012) and Field 14 contains a background dwarf galaxy (Monachesi et al. 2014). The resolved stars from these objects were removed from the field star catalogues for obtaining the colour profile of this galaxy.

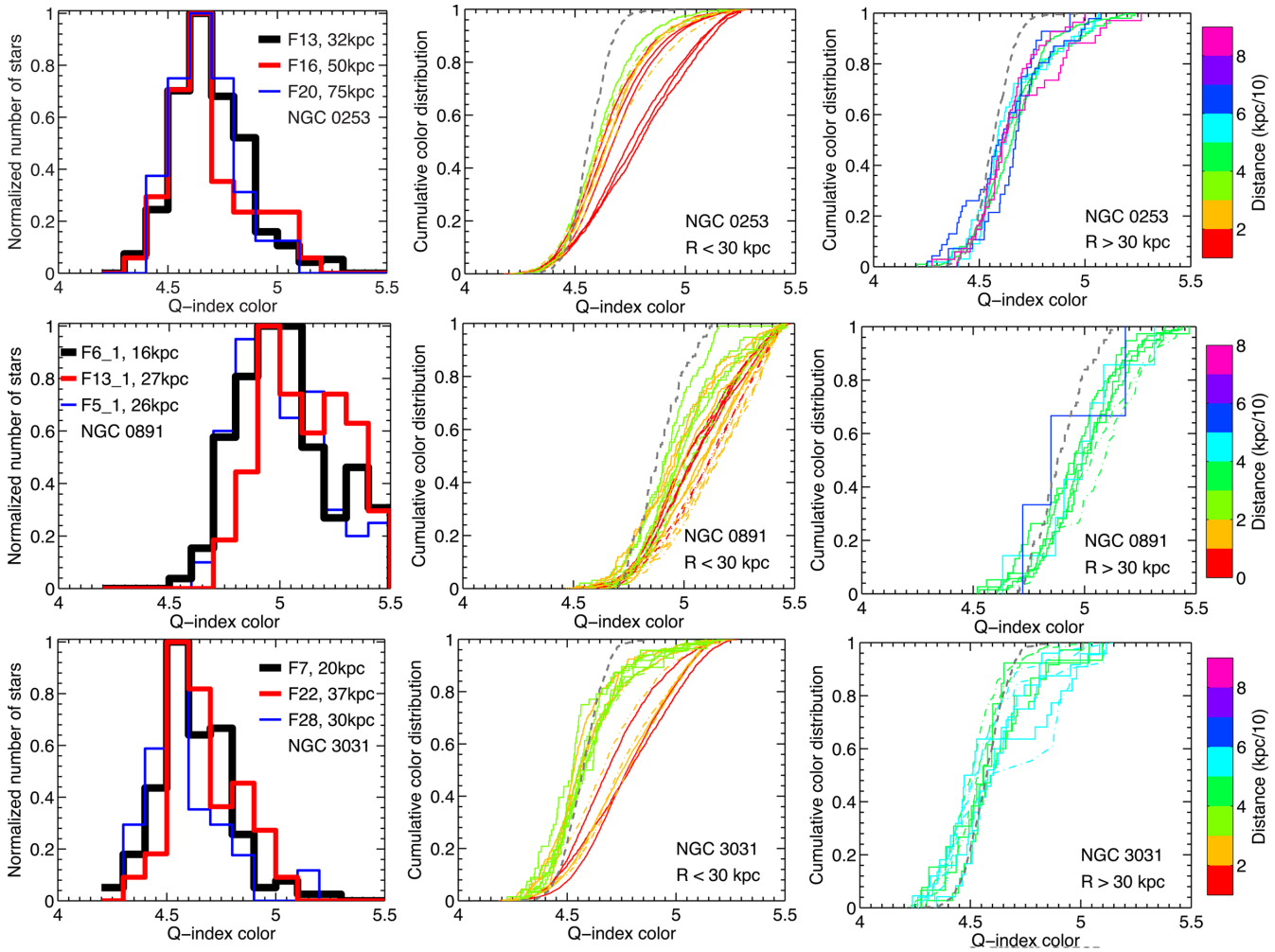

Figure 9. Left-hand panels: a sample of representative colour distribution functions from three fields per galaxy, for NGC 0253, NGC 0891, and NGC 3031. The field numbers and projected distance from the galactic centre in kpc are indicated in each panel. Only stars inside the red selection box shown in Figs 1 to 6 were used to construct these functions. The Q-index colour is obtained by rotating the CMD in such a way that the RGB lies parallel to an isochrone of [Fe/H] $= -1.2$ dex and thus the Q-index colour distribution better reflects the metallicity distribution. Middle and right panels: cumulative colour distributions of each field for fields closer and farther than 30 kpc, respectively. These are colour coded to represent the radial distance of the field to the galactic centre, as indicated in the colourbar. Fields on the major axis are plotted with dash–dotted lines. The grey-dashed line in each panel is a fiducial colour distribution of a 10.5 Gyr old population with metallicities [Fe/H] $= -1.2 \pm 0.3$ dex. The same fiducial model is shown for each galaxy; however, the photometric errors corresponding to each galaxy as well as their RGB selection box were applied to the model in order to construct the cumulative distribution for a fair comparison with the observed data.

linear extensions, having side lengths from ∼9 to ∼14 kpc. In order to obtain colour measurements that represent the properties of stars from similar spatial regions, we divide each field of the more distant galaxies in either three or four radial bins, such that each region for which a colour measurement is made covers ≈ 3 kpc on a side. An exception was made for Field 8 in NGC 0891 and Field 6 in NGC 7814. These fields have about 10 stars in the chosen region selected to calculate the RGB median colour and therefore we do not divide them in radial bins such that we use a statistical sample of stars to measure the median colour.

We see in Fig. 11 field to field variations in the median values of the colours within each galaxy, i.e. colour variations as a function of galactocentric distances. This is observed not only within the first 10 kpc or in fields along the major axis, where colour variations could be attributed to expected metallicity gradients from the disc, but also out to large distances, where stars from the halo are expected to dominate. The degree of scatter within each stellar halo may reflect population variations, predicted by models in which the stellar haloes are built from many small accreted objects. R-S11 showed that photometric differences between magnitude measurements of coincident stars in overlapping fields can account for up to ∼0.04 mag uncertainty in their colours. This systematic uncertainty of 0.04 mag is included in quadrature together with the median uncertainty in the errorbars in Fig. 11. Thus, although some of these colour variations may be partly due to systematics in the data calibration, as maybe e.g. in NGC 0253, the scatter cannot be explained by systematics only in most galaxies.

We also notice that fields along the major axis are typically redder than the minor axis fields at similar galactocentric distances. The redder colours for major axis fields closer than 15 kpc most likely indicate a larger contribution from red more metal-rich disc stars. However, the redder colours for fields at larger distances (seen in NGC 0891, NGC 4565, and NGC 7814) may indicate differences in the stellar halo populations between the minor and major axis

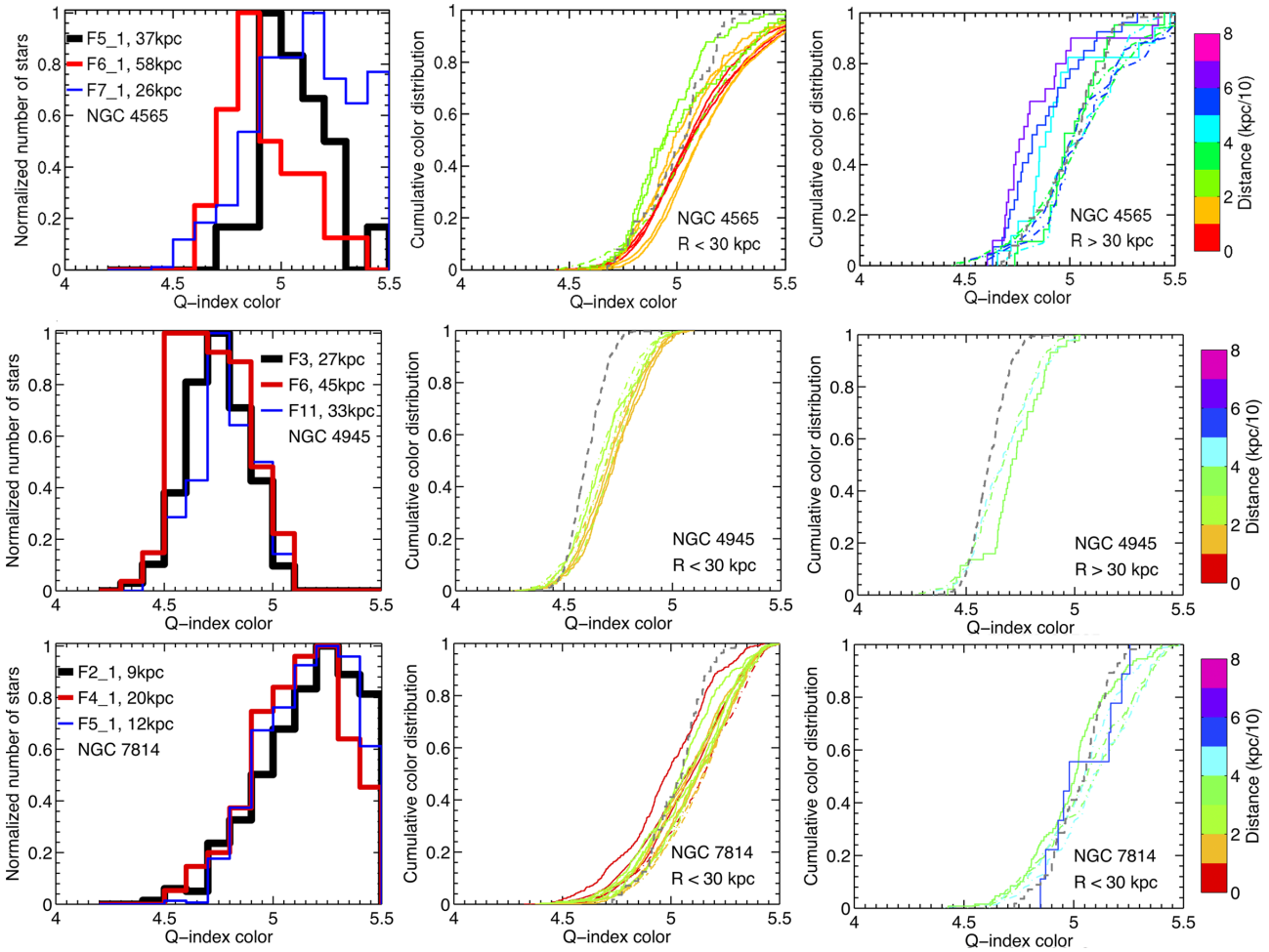

Figure 10. Same as Fig. 9 for galaxies NGC 4565, NGC 4945, and NGC 7814. The subscript 1 in some of the field labels indicate that only one region from that field is used to construct the colour distribution function. This is because the fields of the more distant galaxies have been divided in either three or four regions as explained in Section 5.2.

of the galaxy. A quantitative investigation will require joint fitting of the colours and surface densities of stars, which is deferred to a future work. Nevertheless, we note that the disc scalelengths of NGC 0891, NGC 4565, and NGC 7814 are 4 kpc (Schechtman-Rook & Bershady 2013), 5.5 kpc (van der Kruit 1984), and 4 kpc (Wainscoat, Hyland & Freeman 1990) respectively, larger than the disc scalelengths of NGC 0253, NGC 3031, and NGC 4945, which are 2.1 kpc (Greggio et al. 2014), 2.9 kpc (Barker et al. 2009), and 2.3 kpc (de Vaucouleurs 1964), respectively.

Finally, a first glance of Fig. 11 suggests that two out of six galaxies have a colour gradient (NGC 0891, NGC 4565) whereas four present a rather flat colour profile if we average all the fields per galaxy within a range in radial distances regardless of their different directions. We investigate this further in the next subsection, where only the fields along the minor axis are considered.

5.3 Stellar halo colour profiles: minor axis fields

To study whether there is a colour gradient in the stellar haloes of the GHOSTS MW-mass galaxies, we need first to define a sample of halo stars.

The disc galaxies studied in this work are highly inclined; four out of six are edge-on, and the rest are no more than 25° from edge-on. Therefore, the stellar populations observed along their minor axis fields should mostly sample halo stars with the least possible contamination from disc stars. In order to have a clean stellar halo profile and to avoid the disc as much as possible, we do not use the major axis fields in this section. We assume that the stars observed along the minor axis fields located at galactocentric distances $R > 5$ kpc for the edge-on galaxies (NGC 0253, NGC 0891, NGC 4565, NGC 4945) and $R > 10$ kpc for the highly inclined galaxies (NGC 3031, NGC 7814) represent halo stellar populations.

Fig. 12 shows the minor axis stellar halo colour profile of each galaxy. In order to give a rough quantitative estimate of the magnitude of colour variation with radius, we fit a linear colour gradient to the data. Such a function has no particular physical relevance or motivation, and a variety of radial profile shapes are predicted by models (e.g. Cooper et al. 2010; Font et al. 2011; Tissera et al. 2014). Other parameterizations are possible, but additional complexity seems unwarranted given the number of data points and their uncertainties. The red lines in Fig. 12 show linear fits to the black dots weighted by the uncertainties in the median colours and the number on the top-right corner indicates the slope and its corresponding 1σ uncertainty in units of mag kpc^{-1}. We exclude from the fitting fields that were inside 5 or 10 kpc, shown in the figure as grey dots, according to whether the galaxy is edge-on or highly inclined, respectively, as explained above. Half of the galaxies (NGC 4565, NGC 0891, and NGC 7814) show fits consistent with

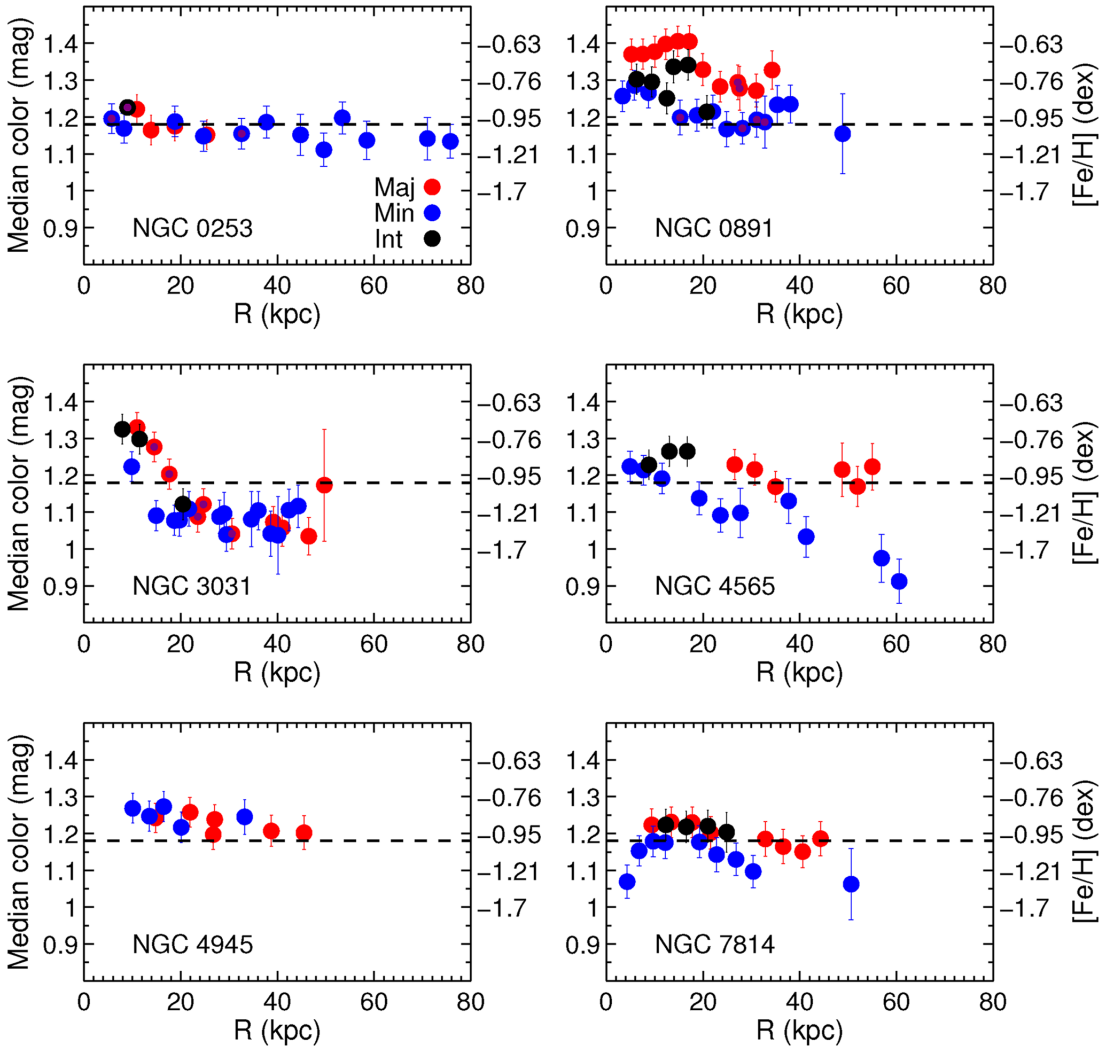

Figure 11. Colour profiles of each individual galaxy using all the fields along the minor (blue dots), intermediate (black dots), and major (red dots) axis of the galaxy. The median colours are calculated using RGB stars selected in a certain magnitude bin such that stars are below the TRGB and above 50 per cent or 70 per cent completeness. The magnitude range from which the median colours are calculated varies from galaxy to galaxy and the faintest magnitude considered is indicated in Table 1. We note that due to the incompleteness of our data at the red end of the NGC 7814 CMDs, the median colours obtained for NGC 7814 are a lower limit of the actual values. Errorbars indicate uncertainties on the median value calculated by bootstrapping the stars sample as well as systematic uncertainties due to calibration. The dashed line at colour = 1.18 represents the average colour profile of the 11 B&J stellar halo model realizations, which lacks a colour gradient (see Section 6.2 and Monachesi et al. 2013 for details about comparing with the models). Purple dots in the profiles of NGC 0235, NGC 0891, and NGC 3031 indicate fields with detected halo substructure discussed in Section 6.3.

stellar halo colour gradients whereas the remaining three galaxies (NGC 0253, NGC 3031, and NGC 4945) have rather flat colour profile. However, it is interesting to note that both NGC 0891 and NGC 4565 show a jump, i.e. a redder colour, in the minor axis colour profile at approximately 38 kpc, which may be related to substructure in these galaxies likely either in the form of a stellar stream or shell. It is also interesting that both major and minor axes profiles increase colour in NGC 891 at roughly that same radius suggesting it is a massive feature, whereas the major axis colour profile in NGC 4565 stays flat while the minor axis decreases over a considerable distance range. We recall that NGC 4565 has a large disc, with a scalelength of 5.5 kpc (van der Kruit 1984), which may influence the colour profile at larger radii on the major axis. Several stellar streams have been detected in NGC 0891 by Mouhcine et al. (2010, see Section 6.3); however, the redder colour at ∼40 kpc cannot be due to any of those streams since their observed field reaches ∼28 kpc from the galactic centre along the minor axis. Our GHOSTS measurements show that there is little population gradient in the stellar haloes of half of the massive disc galaxies in our sample out to ∼60 kpc and half of the galaxies show strong population gradients in their outskirts. We are confident that either gradient or flat behaviour in the colour profiles presented in Fig. 12 are not driven by the disc but rather indicate an actual halo property, due to the above-mentioned selection of stars to obtain the stellar halo profiles.

In Fig. 13, we show the stellar halo colour profiles of all the galaxies together, where we can see the diversity in the colour profiles of massive disc galaxies. The right-hand panel shows the median colours as a function of radius in units of effective radius. This normalizes the differences in galaxy's sizes which may make the comparison between galaxy to galaxy more fair. We note, however, that the effective radius is a major axis/disc property, and may have

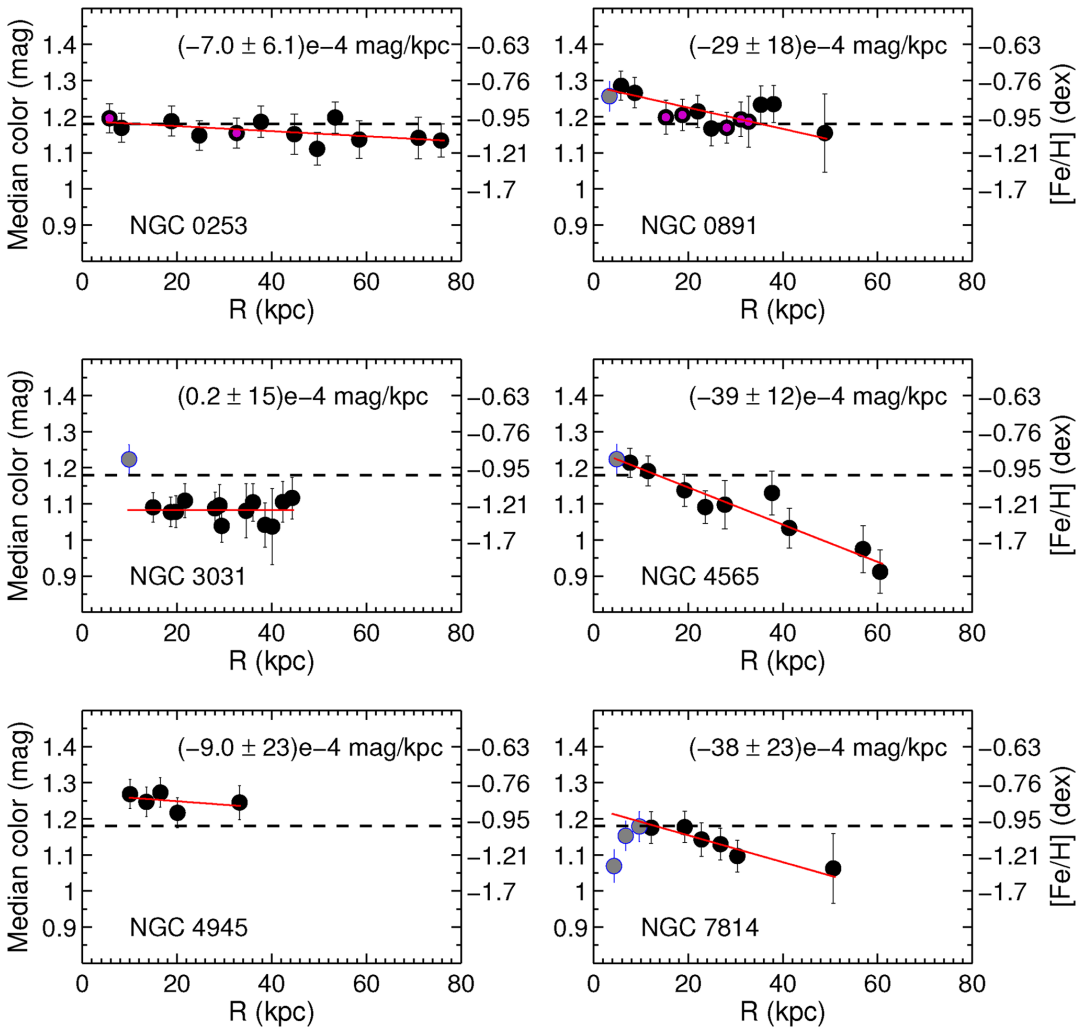

Figure 12. Minor axis colour profiles of each individual galaxy analysed in this work. Median $F606W–F814W$ colours at 0.5 mag below the TRGB are plotted as a function of projected galactocentric distance. The red lines are linear fits to the black dots using fields at $R > 5$ kpc for the edge-on galaxies (NGC 0253, NGC 4945, NGC 0891, and NGC 4565) and at $R > 10$ kpc for the highly inclined galaxies (NGC 3031 and NGC 7814). Fields that were not used in the fit are shown as grey dots. The slope of each fit and its corresponding uncertainty are indicated in each panel. We note that due to the incompleteness of our data at the red end of the NGC 7814 CMDs, the median colours obtained for NGC 7814 are a lower limit of the actual values. Half of the galaxies show colour gradients, which we interpret as metallicity gradients, whereas half show flat colour profiles, indicative of a lack of metallicity gradient. The right-hand y-axes indicate the [Fe/H] values that the colours correspond to, calculated from the relation derived by Streich et al. (2014) and assuming $[\alpha/\mathrm{Fe}] = 0.3$. The metallicities [Fe/H] will be lower or higher for a given colour in case of $[\alpha/\mathrm{Fe}]$ larger or lower than 0.3, respectively. The dashed line at colour = 1.18 represents the average colour profile of the 11 B&J stellar halo model realizations, which lacks any colour gradient (see Section 6.2 and Monachesi et al. 2013 for details about comparing with the models). Purple dots in the profiles of NGC 0235 and NGC 0891 indicate fields with detected halo substructure discussed in Section 6.3.

little to do with the stellar halo properties. Since the galaxies studied in this work are all MW-like galaxies, we find that there is a wide range in halo colours for galaxies of similar mass and luminosity.

5.4 Width of the colour distributions

The widths of the colour distributions provide an idea of the range in colours, and as we argue later metallicities, at any given radius. To quantify this, we use the cumulative colour distribution function of each field shown in Figs 9 and 10. We calculate the Q-index colour range that is within 68 per cent around the median colour, i.e. between the 0.16 and 0.84 values in the cumulative percentage of stars.

Fig. 14 shows the Q-index colour distribution widths as a function of radius for each galaxy. The errorbars indicate the uncertainties on the estimated widths due to the photometric errors. These errors widen the intrinsic colour distribution and may bias our results owing to the different photometric uncertainties for the different galaxies. For each galaxy, we estimate the width uncertainty on each field as follows. We generate 1000 colours per star, which are randomly picked from a distribution of colours. The distribution of colours is centred at the star's observed colour with a 1σ spread corresponding to its photometric error, as derived from the ASTs. We then computed 1000 colour distribution functions and the standard deviation of their colour widths represent the field's colour width uncertainty.[9] We see that the colour widths remain generally

[9] While this procedure clearly overestimates the individual colour distribution width estimates, it does allow estimation of the variation in the widths from iteration to iteration, i.e. the uncertainty in the colour width.

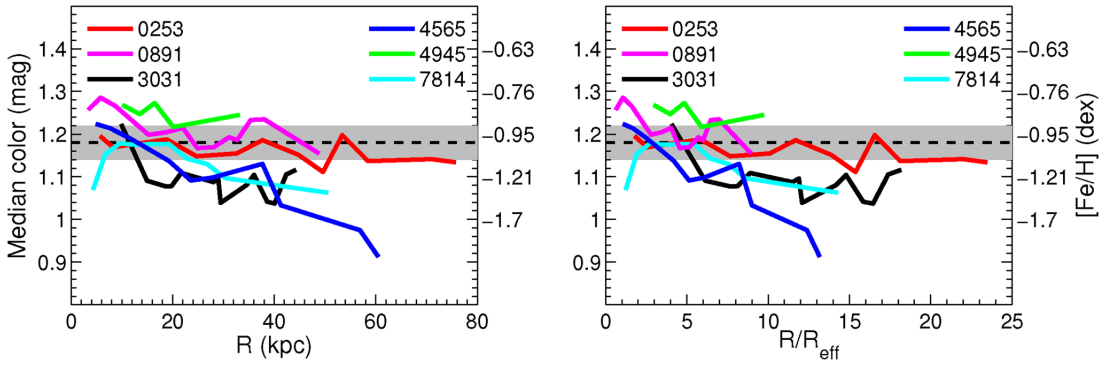

Figure 13. Colour profiles of all the galaxies showing only the minor axis fields, as in Fig. 12, as a function of galactocentric distance in kpc (left) and in units of effective radius (right). The black-dashed line indicates the average colour profile of the 11 B&J stellar halo model realizations and the shaded area represents the 1σ model-to-model scatter from the average.

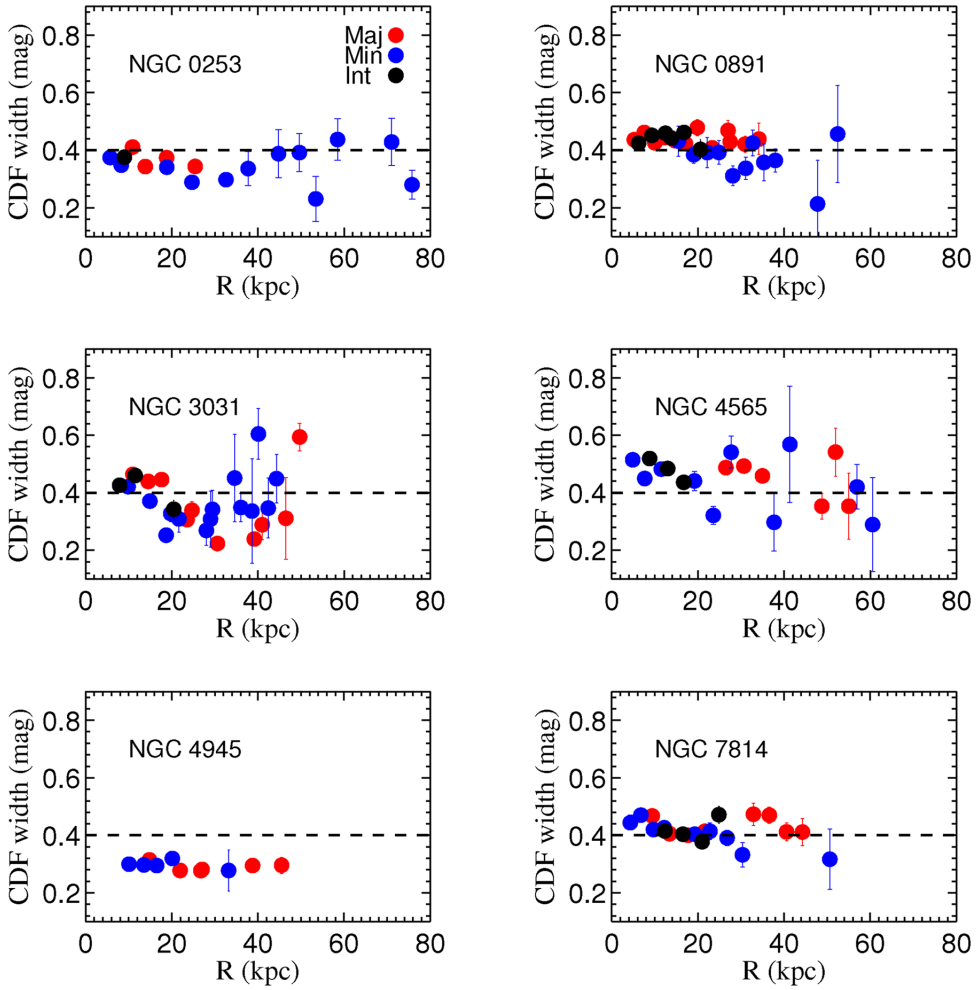

Figure 14. Width of the Q-index colour distribution functions as a function of projected galactocentric distance for each galaxy. Red, blue, and black dots indicate the width value for fields along the major, minor, and intermediate axis, respectively. The errorbars represent the uncertainties on the estimated widths obtained using the photometric errors of each star's colour as derived from the ASTs. The dotted line at width value of 0.4 is the same in all panels to help visualize differences among the galaxies.

constant for most of the radius coverage. There are nevertheless variations from field to field. In particular, for NGC 0253, NGC 3031, and NGC 4565, the width of the colour distributions becomes larger in the outer fields. This would imply a larger range in colours at large radii. It is possible that this reflects artificial broadening of the colour distribution from the larger fraction of contaminants in low stellar density outer fields; it is also possible that this reflects actual metallicity variation in the outer parts of galaxy haloes.

We note that the colour distribution widths for the inner parts of some galaxies (NGC 3031, NGC 4565, NGC 7814, and NGC 0253) are also somewhat broadened at radii less than 15 kpc, compared to their widths at 15 to 40 kpc. We attribute this to contributions

from metal-rich disc stars with some possible contribution from substructure that has been accreted, especially for the edge-on galaxies. These values, however, are a lower limit by construction because the RGB stars selected to generate the colour distribution function were chosen to maximize the contribution from halo stars. Metal-rich disc RGB stars that are significantly redder than the median halo colour are outside the selection box and thus the actual width is likely much wider for the disc fields.

Fig. 14 also shows that there are galaxy-to-galaxy differences in the colour distribution widths. Some galaxies have a larger range of colours per field than others, likely reflecting their different accretion histories.

6 DISCUSSION

In this section, we discuss our results and compare them with other observations of stellar haloes as well as with models of stellar halo formation.

Our results are presented in terms of median colours of RGB stars as a function of projected galactocentric distances. However, because the colours of the RGB stars are more sensitive to metallicity than to age and because there is a direct relation between RGB colours and metallicities (see e.g. Streich et al. 2014, and references therein), one can assume that the colour profiles presented in the previous section reflect metallicity profiles. This assumption will allow us to compare our results with other work in which metallicities of individual fields and/or metallicity profiles of stellar haloes are constructed.

To obtain metallicities from the median RGB colours, we use the observational relation between the *HST* colours $F606W - F814W$ and metallicities derived by Streich et al. (2014). They use a sample of globular clusters observed as part of the ACS Globular Cluster Survey (Sarajedini et al. 2007; Dotter, Sarajedini & Anderson 2011) and relate their RGB colours at the same absolute magnitude as we do (i.e. 0.5 mag below the TRGB) with their metallicities. They find a clear relation between metallicity and RGB colour. However, the metallicities obtained from RGB colours have large uncertainties. Streich et al. (2014) estimate a lower uncertainty of 0.3 dex for metallicities derived for colours $F606W - F814W < 1.2$, whereas metallicities derived for colours redder than 1.2 have a 0.15 dex uncertainty. A metallicity scale is shown on the right-hand *y*-axis of Figs 11–13 to indicate the metallicities that the colours correspond to. We assume $[\alpha/\mathrm{Fe}] = 0.3$ to derive [Fe/H], since this is the typical value for halo stars in the MW (e.g. Venn et al. 2004; Ishigaki, Chiba & Aoki 2012) as well as in M31 (Vargas et al. 2014). In addition, Robertson et al. (2005) and Font et al. (2006a) argue that typical halo stars should be alpha enriched to approximately this degree, by combining cosmologically motivated stellar halo models with a chemical evolution model, reflecting that most halo stars were accreted at early times before redshift one. Higher or lower values than $[\alpha/\mathrm{Fe}]$ will result in lower or higher [Fe/H], respectively, for a given colour.

6.1 Comparison with other observed stellar haloes

Given a direct relation between RGB colours and metallicities, our results suggest that three out of six stellar haloes studied present a metallicity gradient. Moreover, we likely observe field-to-field variations in the median metallicity of the stars in the outer regions, as expected if the halo is built up by accretion of different satellites. We also find that all of the GHOSTS galaxies have relatively high median metallicity in their haloes, in some cases higher than [Fe/H] ~ -1.2 dex out to $\sim$50–70 kpc.

For the MW, the stellar halo metallicity gradient has been a controversial topic for several decades. Some pioneering works using globular clusters as tracers of the Stellar Halo have claimed both the existence of a metallicity gradient (Harris & Canterna 1979) as well as the lack of it (see e.g. Armandroff, Da Costa & Zinn 1992; Alfaro, Cabrera-Cano & Delgado 1993, and references therein). Carollo et al. (2007, 2010) used orbital properties of local halo stars from Sloan Digital Sky Survey (SDSS) data to measure the metallicity of the local halo and inferred from this sample the metallicity of the outer halo. They claimed that the MW halo has a strong negative metallicity gradient, with the median metallicity changing from -1.6 dex in the solar neighbourhood to -2.2 dex beyond 15 kpc. However, these results suffer from important biases. Their magnitude-limited sample includes only luminous low-metallicity stars at large distances, imposing an artificial metallicity gradient (Schönrich et al. 2011). This emphasizes the need for more representative samples of distant halo stars, a requirement that only relatively recently has been met. Sesar et al. (2011) use near-turnoff MS stars out to $\sim$35 kpc from Canada–France–Hawaii Telescope observations to infer no metallicity gradient. Recently, Xue et al. (2015) use a sample of SEGUE K-giants halo stars fairly sampling 10 to 50 kpc to infer a weak metallicity gradient. Current (e.g. *Gaia* mission, Apache Point Observatory Galactic Evolution Experiment, Large Sky Area Multi-Object Fiber Spectroscopic Telescope) or upcoming (4-metre Multi-Object Spectroscopic Telescope, WHT Enhanced Area Velocity Explorer, Dark Energy Spectroscopic Instrument, and Large Synoptic Survey Telescope) efforts will allow further refinement of these estimates.

M31 is easier to study than the MW because we can have an external and complete global view of it, where a single distance for all its stars is assumed. At the same time, due to its proximity, M31 can be studied in great detail. Stellar population variations in M31's halo have been found in several studies (see e.g. Brown et al. 2006; Richardson et al. 2008; McConnachie et al. 2009). In addition, recent work by the Pan-Andromeda Archaeological Survey (Ibata et al. 2014) and Spectroscopic and Photometric Landscape of Andromeda's Stellar Halo (Gilbert et al. 2014) surveys have shown very clearly that there is a strong metallicity gradient in the stellar halo of M31 if observed over large enough radial ranges. The results from PAndAS are based on the colours of resolved RGB stars, whereas SPLASH survey uses both spectroscopic and photometric data of RGB stars, being able to isolate kinematically a sample of M31's halo stars in a statistical manner. The metallicity profile of M31's stellar halo shows a continuous gradient from 9 to 100 kpc, with the median metallicity gradually decreasing from [Fe/H] ~ -0.47 at 9 kpc to [Fe/H] ~ -1.4 at 100 kpc, for $[\alpha/\mathrm{Fe}] = 0$; metallicities will be $\sim$0.22 dex lower if $[\alpha/\mathrm{Fe}] = 0.3$, typical for halo stars, is assumed instead.

Mouhcine et al. (2005a,b,c) presented the first study of halo metallicity in spiral galaxies outside the Local Group. They resolved individual RGB stars in the haloes of eight nearby disc galaxies and analysed their metallicities using the colours of the RGB stars. Among the galaxies studied by Mouhcine et al. (2005a) four are low-mass, low-luminous galaxies and four are MW-like galaxies. We compare our results with their results from the latter group, which is the type of galaxies studied in this work. They analysed one field per galaxy using the WFC2 onboard the *HST*, located between 3 and 13 kpc in projected distance along the galaxy's minor axis. Their data are shallower than GHOSTS data by one or two magnitudes. Nevertheless, they were able to reach magnitudes

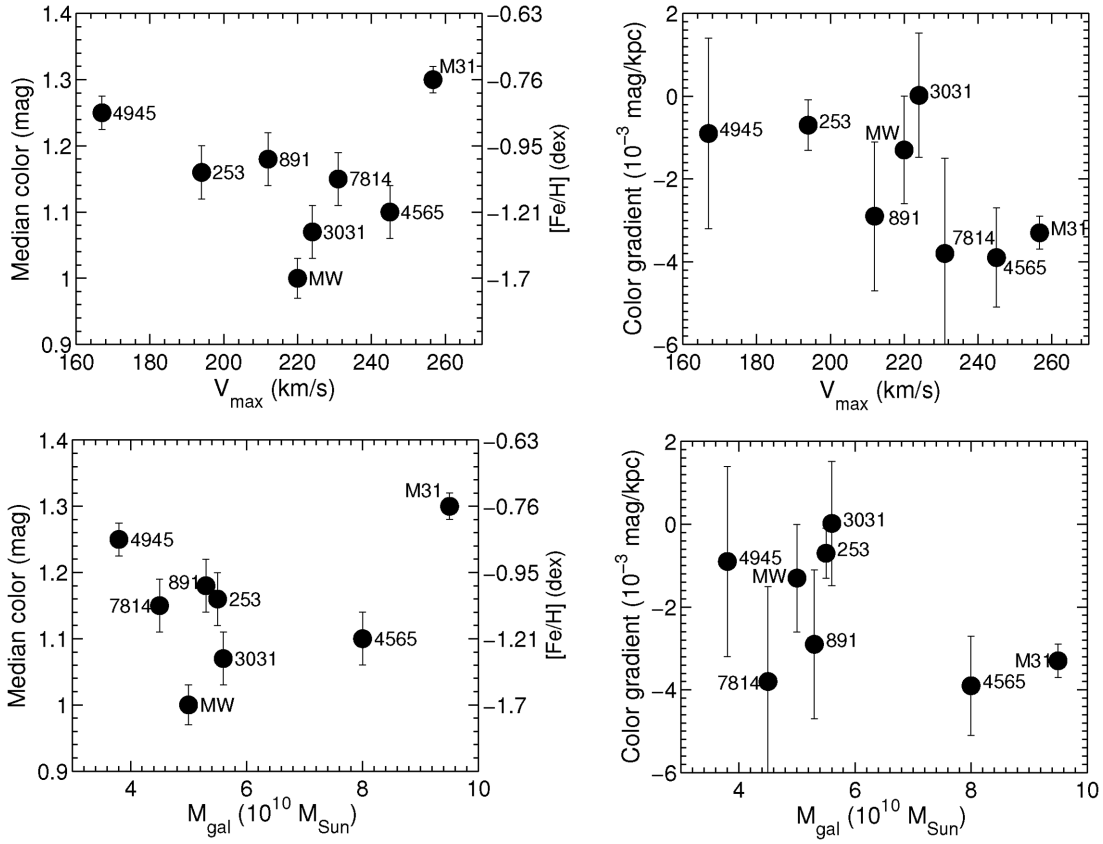

Figure 15. Halo median colours/metallicities (left-hand panels) and slopes of colour gradients (right-hand panels) as a function of V_{max} (top panels) and total stellar mass for the eight massive disc galaxies for which this information is available, i.e. the six GHOSTS galaxies analysed in this work in addition to our own MW and M31. The median colour values are taking at 30 kpc along the minor axis of these galaxies. For the MW and M31, we assume a median metallicity of −1.7 dex (Sesar et al. 2011; Xue et al. 2015) and −0.76 dex (Gilbert et al. 2014, with an additional −0.213 dex to account for the alpha enhancement of 0.3 assumed in this work) respectively, which were transformed into colours using Streich et al. (2014) relationship. Similarly, the colour gradients for MW and M31 were obtained from their metallicity values at 10 and 30 kpc. There is a significant scatter in stellar halo colour/metallicity and colour/metallicity gradient in a narrow range of stellar mass or rotation velocity. We see no significant trend in correlation between these quantities and either V_{max} or total stellar mass.

down to 1 or 1.5 mag below the TRGB. Mouhcine et al. (2005b) derived a colour–luminosity relation between the halo colour and luminosity of the host galaxy. Moreover, they concluded that massive disc galaxies have haloes with rather high metallicities, surprisingly more metal rich than what is thought typical of the MW halo at the same radii ([Fe/H] $\sim -0.6/-1.0$ versus $[Fe/H]_{MW} \sim -1.6$). Three out of the four massive galaxies in their sample are studied in this work too, namely NGC 253, NGC 3031, and NGC 4945. We find that our results are consistent with their estimated metallicities, when comparing our colour measurements at the locations of their fields. The most important difference between GHOSTS and Mouhcine et al. (2005a) observations is that they use a single field per galaxy whereas GHOSTS observes several fields per galaxy which thus allows us to obtain colour differences and gradients as a function of radius. GHOSTS also reaches ∼55 kpc further away from the galactic centre than Mouhcine fields, assuring that we have no disc contamination along the minor axis. Interestingly, we find that the three galaxies in common between Mouhcine et al.'s sample and ours have a flat colour/metallicity gradient. Thus, the metallicity estimated by Mouhcine et al. (2005c) in one field can be applied to the outer regions in those galaxies. Moreover, we show in Fig. 13 that even in the outer regions at minor axis radii of $R \sim$ 70 kpc in projection, we can find RGB halo colours consistent with metallicities similar or higher than [Fe/H] $= -1.2$ dex. In addition, we find a wide range in stellar halo colours (from 0.9 to 1.3) which translate into metallicities between −0.6 dex and −1.7 dex.

We explore this further in Fig. 15 where the median colour of the stellar haloes at 30 kpc and slopes of their colour gradients are plotted as a function of both V_{max} (maximum rotational velocity) and total stellar mass for all the eight massive disc galaxies for which this information is available, i.e. the six GHOSTS galaxies presented in this work in addition to the MW and M31. The median colour values at 30 kpc for the MW and M31 were estimated using the Streich et al. (2014) relationship, assuming $[\alpha/Fe] = 0.3$. The metallicity at 30 kpc of M31's halo is from Gilbert et al. (2014)[10] and the metallicity at 30 kpc of the MW's halo is the mean metallicity between the value reported in Sesar et al. (2011) and Xue et al. (2015), i.e. [Fe/H] $= -1.7$ dex. Stellar masses for the GHOSTS galaxies were estimated using K-band luminosities, coupled with a typical K-band mass-to-light ratio of $M/L = 0.6$, typical of massive spiral galaxies, following Bell & de Jong (2001) using a universally applicable Chabrier (2003) stellar IMF. Luminosities were calculated using K-band total magnitudes from Jarrett et al. (2003), in

[10] We note that the [Fe/H] reported in Gilbert et al. (2014) were derived assuming no alpha enhancement. We have corrected their reported [Fe/H] metallicities for the assumed $[\alpha/Fe] = 0.3$.

conjunction with the distances presented in Table C1. Such masses carry at least 30 per cent uncertainties, and potentially suffer from larger systematic error if assumptions underlying their calculation are incorrect, e.g. if the stellar IMF varies from galaxy to galaxy. Despite these uncertainties, these masses are useful in order to build intuition about how these galaxies compare to larger samples of galaxies, e.g. from the SDSS (e.g. Kauffmann et al. 2003) that have stellar mass estimates but lack accurate measures of rotation velocity. Stellar masses for the MW and M31 are from Bovy & Rix (2013) and Sick et al. (2015), respectively. We find that there is a factor of 5 scatter in stellar halo metallicity and a significant scatter in metallicity gradient amongst these eight galaxies, illustrating a considerable diversity in halo properties in a narrow range of galaxy mass and rotation velocity. There is no correlation between $V_{\rm max}$ and colour/metallicity and a possible weak trend between the colour gradient and $V_{\rm max}$. The Spearman rank correlation coefficient between the $V_{\rm max}$ and colour/metallicity is -0.0952 whereas the coefficient is -0.6429 when the colour gradient is plotted against $V_{\rm max}$. This indicates a larger correlation of $V_{\rm max}$ with colour gradient although, from its significance of 0.12, there is an $\sim$10 per cent probability that these quantities are drawn from an uncorrelated data set. Correlation of the same quantities with total stellar mass is even weaker (bottom panel of Fig. 15).

So far, we have information about the colour/metallicity profiles of eight disc galaxies: MW, M31, and the six GHOSTS disc galaxies presented here. Four out of eight stellar haloes show clear negative metallicity gradients whereas three present rather flat profiles, and one (our own MW) may or may not have a stellar halo metallicity gradient. Regardless of whether there is a metallicity gradient or not, the average colour of *all* stellar haloes considered implies a higher average metallicity than that of the MW's halo, although a recent work by Janesh et al. (2015) indicated that there are a significant number of stars in their SEGUE halo sample with [Fe/H] > -1. In addition, one should keep in mind that comparing the results obtained from different observations is not always straightforward. These arise generally from different sample of halo stars (or different halo tracers), methodology and techniques used to derive the results and often even the definition of what is considered the stellar halo of the galaxy varies. All these differences may complicate a direct comparison of results from the literature.

We conclude from this comparison that the haloes of massive disc galaxies appear to show a great diversity in their colours/metallicities as well as in the behaviour of their colour/metallicity profiles. In addition, notwithstanding the modest sample size, there is no strong correlation between their halo colour/metallicity or gradient with galaxy's properties such as rotational velocity or stellar mass.

6.2 Comparison with models of stellar halo formation

In Monachesi et al. (2013), we have quantitatively compared the colour profile obtained for NGC 3031 with the cosmologically motivated models from Bullock & Johnston (2005, hereafter BJ05). The stellar haloes in BJ05 are built entirely from the merger and disruption of satellite galaxies within an ΛCDM cosmology, thus they only have an accreted component. The BJ05 models are so-called hybrid models. Star particles in subhaloes generated using high-resolution *N*-body simulations are painted on to pure dark matter particles such that their luminosity function follows a King profile. A cosmologically motivated semi-analytic model of galaxy formation is used to assign stellar properties to the painted particles (see also Robertson et al. 2005; Font et al. 2006a).

In order to have a faithful comparison between the models and our observations, we converted the star particles of BJ05 into stars and built synthetic CMDs of the 11 stellar haloes generated using Padova luminosity functions (Marigo et al. 2008; Girardi et al. 2010) and the IAC-STAR code (Aparicio & Gallart 2004), as explained in detail in Monachesi et al. (2013). We excluded from our analysis stellar populations that belong to surviving satellites, i.e. stellar particles that are still bound to their original progenitor. We then built *HST*-like fields along different directions and different projected distances on the sky of each stellar halo and simulated the observational effects in each synthetic *HST*-like CMD per field using the results from the ASTs. We constructed colour profiles and colour distribution functions in the exact same way as done with the observations and we averaged the results obtained from each of the 11 realizations. We refer the reader to Monachesi et al. (2013) for a detailed description of this process.

In each panel of Fig. 13, we show the resulting average colour profile from the BJ05 models as a black-dashed line. The shaded area indicates the 1σ model-to-model deviations from the average. The BJ05 models do not predict a colour gradient in the stellar halo. This may not be incredibly surprising, since it is known that the metallicity profiles of B&J models lack large-scale gradients (Font et al. 2006b). Nevertheless, given the wide age spread that there is in the BJ05 models as well as the pencil-beam nature of our observations, a quantitative direct comparison of the models with our data using colour profiles of RGB stars was required.

We can see from Fig. 13 that the colour profiles of most of the massive disc GHOSTS galaxies are broadly consistent with that of the BJ05 models. Half of our galaxies lack a detectable colour gradient, and the predicted ages and metallicities of the models yield colours that broadly agree with the colours of GHOSTS galaxies. Cooper et al. (2010) presented six stellar haloes generated using a different type of hybrid method than BJ05 and from higher resolution *N*-body dark matter simulations, also found mostly flat metallicity profiles in the stellar haloes (see also Gómez et al. 2012). They show, however, that a diversity of metallicity profile behaviour can be obtained, from flat to gradients or sharp changes, when a stellar halo is built purely from accretion of satellite galaxies. The differences in the metallicity profiles originate from the different accretion histories of the simulated galaxies. In general, there is little or no metallicity gradient when many satellites contribute comparably in mass to the final halo, whereas metallicity profiles show gradients or sharp variations when only one or two massive systems contribute significantly to the final halo.

On the other hand, cosmological hydrodynamical simulations of galaxies that model both dark matter and baryon particles, i.e. these galaxies contain an *in situ* as well as an accreted component, predict generally strong negative gradients in their metallicity profiles. Font et al. (2011) have analysed $\sim$400 massive disc galaxies using the cosmological hydrodynamical simulations Galaxies-Intergalactic Medium Interaction Calculation of moderate resolution and showed that, on average, the stellar halo metallicity gradually decreases out to $\sim$60 kpc, with the deepest decline over the range of $20 < R < 40$ kpc and a decrease of only 0.1 dex from 60 kpc out to 200 kpc. They argue that the change in slope at $R \sim 30$ kpc is associated with the transition region at which the accreted component of stellar haloes starts to dominate over the *in situ* component (dominant at $R < 30$ kpc). The strong metallicity gradient as an *ubiquitous feature* of the simulated galaxies by Font et al. (2011) is *not supported by our observations*. Only half of our galaxies show colour gradients, which reflect metallicity gradients.

Tissera et al. (2013, 2014) analysed a suite of six highly resolved MW-mass galaxies in a cosmological hydrodynamical simulation. Although all their metallicity profiles present gradients within the inner ∼20 kpc, which are not seen in some of the GHOSTS haloes, two out of six show flat metallicity profiles outside this range and out to ∼100 kpc whereas the remaining four continue to have negative gradient metallicity over the entire radii. Tissera et al. also showed that the transition radius between inner and outer halo populations (divided according to an energy criteria) is at $R \sim 15$–20 kpc. They moreover indicated that differences in the features exhibited in the metallicity profiles obtained reflect their galaxy different assembly history. According to their simulations, metallicity differences between the inner and outer haloes would generally require a contribution of *in situ* stars. However, metallicity differences between inner and outer regions can also be observed if only accreted stars are considered, in the case of a halo whose assembly history has contributions from massive satellites. In addition, they find that the fraction of accreted stars in the inner 20 kpc of their haloes varies from ∼30 to ∼60 per cent. They then predict that the system-to-system scatter in the *in situ* mass fraction is large and spans over a factor of 4.

Pillepich, Madau & Mayer (2015) have presented a very high-resolution cosmological hydrodynamic simulation of a late-type spiral galaxy, 'Eris', close MW analogue. They find a positive metallicity gradient between the inner, $r < 20$ kpc, and outer halo, with a median metallicity of $[Fe/H] = -1.5$ dex within 20 kpc from the centre and $[Fe/H] = -1.3$ dex beyond this radius. This seems to be in contrast with most of the MW observations and the authors claim that this difference may be due to the different assembly history between Eris and the MW.

We note that the simulations by Tissera et al. and Pillepich et al. seem to reproduce well some of the observations. The difference between their and Font et al. (2011) predictions might be due to resolution. It is thus encouraging that the observations are a closer match to the higher resolution (and therefore likely more realistic) simulations. Nevertheless, with only six simulated stellar haloes from high-resolution hydrodynamical models it is not possible to assess the relevance of these results against the possibility of large halo-to-halo variations. Large statistics of high-resolution cosmological hydrodynamical simulations, such as the recently generated Evolution and Assembly of GaLaxies and their Environments (Schaye et al. 2015) and Illustris (Pillepich et al. 2014)[11] simulations, are required to be able to quantify the scatter in halo-to-halo properties. A faithful comparison between the results from such simulations and our observations must be done in order to assess how important the *in situ* component of stellar haloes is and what fraction of galaxies show a large contribution from *in situ* halo stars.

6.3 Panoramic view of GHOSTS galaxies

We gain exquisite information about the stellar populations as well as robust detection of halo stars when using *HST* observations to study stellar haloes of nearby galaxies. However, mapping an entire stellar halo from space is not yet feasible; only small-pencil beam regions can currently be explored. Given the abundant substructure observed (see e.g. Bell et al. 2008; McConnachie et al. 2009; Martínez-Delgado et al. 2010; Ibata et al. 2014) and predicted to be in stellar haloes (see e.g. BJ05 Cooper et al. 2010), our view of their stellar properties may be biased if *only* one small region is sampled (e.g Mouhcine et al. 2005b). In other words, observations of tiny regions around galaxies may not necessarily represent the global picture of their stellar halo. This situation is worse when we look at the nearest galaxies, where each *HST* FoV represents a few kpc^2.

The GHOSTS observations attempt to overcome this issue by placing several *HST* pointings along the different axes of each galaxy such that our results are representative of a relatively large portion of the stellar halo. It is thus very unlikely that *all* our observations would only sample, e.g. the properties of one single stellar stream. For the farthest galaxy in this study, NGC 7814, each *HST* FoV covers a 14 kpc × 14 kpc area.

Nevertheless, even with information from various halo regions, *HST* pencil-beam observations should ideally be complemented with a panoramic view of each studied galaxy to have a global picture of the corresponding stellar halo. We note that panoramic view observations of stellar haloes from ground-based telescopes suffer from strong foreground and background contamination. Most of the panoramic view of galaxies are obtained with integrated light instead of resolved stars, with which is not possible to constrain the halo stellar populations. Ground-based observations of resolved stellar populations, on the other hand, are heavily contaminated from unresolved background galaxies which, due to the lower resolution of these observations, are difficult to distinguish. The lower resolution leads generally also to severe crowding issues (see e.g. Bailin et al. 2011, most of the RGB stars they detected from ground-based observations of NGC 0253 were blends). It is also difficult to reach deeper, hence fewer RGB stars per kpc^2. Therefore, their surface brightness sensitivity is effectively lower than the one reached by *HST* observations and constraining the stellar populations of faint features as the extended stellar halo is compromised when using ground-based observations. In what follows, we discuss the sample of GHOSTS galaxies presented in this work with complementary panoramic imaging and briefly highlight the findings from wide-field imaging. NGC 4945 and NGC 4565 currently lack panoramic imaging of their haloes.

(i) NGC 0253 has been observed using the Visible and Infrared Survey Telescope for Astronomy telescope (Greggio et al. 2014). These observations resolve individual AGB and RGB stars that belong to the halo of NGC 0253 out to ∼40 kpc along the galaxy's minor axis. Their stellar map shows a prominent southern shelf (also observed in Beck, Hutschenreiter & Wielebinski 1982; Davidge 2010; Bailin et al. 2011) and a newly discovered symmetrical feature on the north side. From the 14 *HST* fields probing the halo of NGC 253 (from Field 7 to Field 20), only three fall in substructures. Fields 9 ($R \sim 6$ kpc on the minor axis) and 10 ($R \sim 10$ kpc on an intermediate axis) are on the southern shelf and Field 13 ($R \sim 33$ kpc on the minor axis) falls on the north substructure. We show in a follow-up paper that there is an overdensity in the star counts that we obtain from GHOSTS in Field 13 (Harmsen et al., in preparation) although its colour does not seem to deviate from that of the other fields.

(ii) Mouhcine et al. (2010) presented a panoramic view of NGC 0891. They resolved RGB stars and constructed a surface density map of NGC 0891 across the surveyed area, covering 90 kpc × 90 kpc. Abundant stellar substructure was found in the outskirts of

[11] Although we note that the Illustris, Eris, and Tissera et al. (2014) stellar haloes are much more massive than observed haloes (see e.g. Bell et al. 2008 for the MW and Ibata et al. 2014 for M31), carrying typically more than 20 per cent of a galaxy's mass, in some cases even half of it. While the successful simulation of such a large ensemble is a tremendous achievement, such simulations appear to be far from the large dynamic range required to successfully model stellar haloes accurately.

the survey, including a giant stream and four other arcing streams that loop around the galaxy extending up to ∼40 kpc west and ∼30 kpc east. In addition, they observed a thick cocoon-like stellar structure surrounding the galaxy extending along the minor axis (or vertically) up to ∼15 kpc and along the major axis (or radially) up to ∼40 kpc. Our GHOSTS fields are placed on the east side of the galaxy, thus avoiding the giant stream and other streams that extend up to 40 kpc on the west. Fields 5 ($R \sim 30$ kpc on the minor axis) and 6 ($R \sim 20$ kpc on the minor axis), however, overlap with two regions of streams (one stream each field). Fields 12 ($R \sim 25$ kpc on the major axis) and 13 ($R \sim 30$ kpc on the major axis) likely contain material from the giant stellar stream along the major axis (Holwerda et al., in preparation). In addition, Field 1 ($R \sim 6$ kpc) along the minor axis and all the fields along the major axis, except Field 13, overlie in the extended envelope surrounding the galaxy, which seem to be present out to ∼10 kpc along the minor axis. We see a distinct colour difference between major and minor axes at a given radius out to 30 kpc, where the colour on the major axis at 30 kpc is similar to the colour on the minor axis at 10 kpc. This might suggest that the 'cocoon' extends out to 30 kpc along the major axis and 10 kpc along the minor axis.

(iii) A wide field of resolved stars covering an area of ∼0.3 deg^2 in the northern half of NGC 3031 (M81) was presented by Barker et al. (2009). The resolved RGB star counts allowed them to detect a faint, extended component beyond the bright optical disc. No stellar streams have been reported or shown in this study, although recent Hyper Suprime-Cam data show evidence of a stellar stream of RGB stars connecting M81 with its neighbouring galaxy M82 (Okamoto et al. 2015). Our GHOSTS Fields 2, 3, 4, 13, and 14 along the major axis of M81 would show contributions from such stream material. Nevertheless, we do not use the fields along the major axis to obtain conclusions about the colour gradient of M81's stellar halo.

(iv) NGC 7814 was observed with small (telescope aperture $D =$ 0.1–0.5 m) robotic telescopes Martínez-Delgado et al. (2010) and panoramic view does not show any signs of tidal streams (Martínez-Delgado, private communication).

7 SUMMARY AND CONCLUSIONS

We analyse the halo stellar populations of six MW-mass disc galaxies. New *HST*/ACS and *HST*/WFC3 data from the GHOSTS survey are used in this work as well as *HST*/ACS data introduced in the GHOSTS data paper by R-S11. Several fields along the principal axes of each galaxies were imaged and we were able to construct CMDs of these fields showing halo populations out to ∼50 kpc and in some cases out to ∼70 kpc along the minor axis. The 50 per cent completeness level of the CMDs are reached at one to two magnitudes below the TRGB, depending on the galaxy's distance. The RGB region of the CMDs used for our analyses are mostly free of contaminants such as background unresolved galaxies and foreground MW stars, after selective cuts are applied to the source catalogues.

Using the RGB stars as halo tracers, we obtain their colour distribution in each field/galaxy which provides information on both the dominant colour and the range of colours in each field. We use only RGB stars that are above the ∼50 per cent or 70 per cent completeness level in each galaxy for this analysis. The stellar halo colour profile of each galaxy is derived by utilizing only the median colour information of fields along each galaxy's minor axis, which are assumed to be as clean as possible from disc contaminants. We compare our results with other observations and with models of galaxy formation in a cosmological context.

Here, we summarize our findings and conclusions.

(i) *All* of the galaxies studied in this work have halo stars out to at least 50 kpc and some out to ∼70 kpc. Thus, our observations show that massive disc galaxies ($V_{\rm max} \gtrapprox 170$ km s^{-1}) have very extended stellar envelopes beyond the region where the disc dominates.

(ii) The colour distributions exhibit differences in the range of colours as well as in the dominant colour for different galaxies and even from field to field within a galaxy in some cases (e.g. NGC 0891, NGC 4565).

(iii) The colour profiles, obtained computing the median colour of RGB stars within a magnitude range as a function of radius, indicate field to field variations in colour within each galaxy. This variation cannot be explained solely by systematic uncertainties (since the differences in many cases are larger than the errorbars which include the systematic uncertainties) and thus most likely reflect stellar population variations as a function of galactocentric distance.

(iv) The stellar halo colour profiles obtained using the minor axis fields of three out of six galaxies display a negative gradient, with gradually bluer colour in the outer regions. Three galaxies show flat colour halo profiles (NGC 0253, NGC 3031, NGC 4945) reflecting negligible halo population variations as a function of galactocentric distances.

(v) Given the direct relation between RGB colours and metallicities, we can estimate the metallicity that the measured colours correspond to. We assume $[\alpha/{\rm Fe}] = 0.3$ to estimate the halo metallicity and find that the GHOSTS galaxies have a large range of stellar halo median metallicities at 30 kpc from [Fe/H] ~ -0.8 dex to [Fe/H] ~ -1.5 dex.

(vi) Since there is a wide range in halo colours and metallicities for disc galaxies of similar mass and luminosity, this implies that the colour–luminosity relation derived by Mouhcine et al. (2005c) must have a large scatter in colour. Moreover, we find no strong correlation between the stellar halo median colours/metallicities and either $V_{\rm max}$ or total stellar mass of the galaxy. There may be a trend between colour/metallicity gradient and $V_{\rm max}$ such that galaxies with larger $V_{\rm max}$ have more significant colour/metallicity gradients, although the statistics are poor and there is a 10 per cent probability for these quantities to be drawn from an uncorrelated distribution.

(vii) When comparing our results with cosmologically motivated models of galaxy formation in which stellar haloes are purely built up from accretion events, we find a general good agreement with the observations.

(viii) Cosmological hydrodynamical simulations with varying importance of *in situ* populations dominating to 20 kpc from the disc reproduce some of the observations. They predict that most or all galaxies should have strong negative metallicity gradients, which seems in conflict with half of our sample with little to no metallicity gradient. However, the gradients presented in these simulations are obtained from spherically averaged metallicities. A more appropriate comparison would be between our minor axis colour profiles and the *minor axis* colour and metallicity profiles of hydrodynamical models; this will be presented in a future work.

We conclude that the haloes of disc massive galaxies appear to show great diversity in their colours/metallicities as well as in the behaviour of their colour/metallicity profiles. This reflects the scatter in the halo-to-halo properties predicted by cosmological simulations due to the stochastic process of galaxy formation.

ACKNOWLEDGEMENTS

AM wishes to thank Guinevere Kauffmann for useful comments and discussions as well as Annette Ferguson and David Martinez-Delgado for providing information about the existence (or not) of stellar streams in NGC 3031 and NGC 7814 prior to publication. We wish to thank the anonymous referee for useful comments and suggestions that helped improve this paper. This work was supported by NSF grant AST 1008342 and *HST* grant GO-11613 and GO-12213 provided by NASA through a grant from the Space Telescope Science Institute, which is operated by the Association of Universities for Research in Astronomy, Inc., under NASA contract NAS5-26555. Additionally, some of the data presented in this paper were obtained from the Mikulski Archive for Space Telescopes (MAST). STScI is operated by the Association of Universities for Research in Astronomy, Inc., under NASA contract NAS5-26555. Support for MAST for non-*HST* data is provided by the NASA Office of Space Science via grant NNX09AF08G and by other grants and contracts. DS gratefully acknowledges support from the Cusanuswerk through a PhD scholarship and from the Deutsches Zentrum für Luft- und Raumfahrt (DLR) through grant 50OR1012. We acknowledge the usage of the HyperLeda data base (http://leda.univ-lyon1.fr/). This work has made use of the IAC-STAR Synthetic CMD computation code. IAC-STAR is supported and maintained by the IAC's IT Division. This work used the astronomy & astrophysics package for MATLAB (Ofek 2014).

Facility: *HST* (ACS and WFC3).

REFERENCES

Alfaro E. J., Cabrera-Cano J., Delgado A. J., 1993, ApJ, 402, L53
Anderson J., Bedin L. R., 2010, PASP, 122, 1035
Aparicio A., Gallart C., 2004, AJ, 128, 1465
Armandroff T. E., Da Costa G. S., Zinn R., 1992, AJ, 104, 164
Bailin J., Bell E. F., Chappell S. N., Radburn-Smith D. J., de Jong R. S., 2011, ApJ, 736, 24
Barker M. K., Ferguson A. M. N., Irwin M., Arimoto N., Jablonka P., 2009, AJ, 138, 1469
Beck R., Hutschenreiter G., Wielebinski R., 1982, A&A, 106, 112
Bell E. F., de Jong R. S., 2001, ApJ, 550, 212
Bell E. F. et al., 2008, ApJ, 680, 295
Bell E. F., Xue X. X., Rix H.-W., Ruhland C., Hogg D. W., 2010, AJ, 140, 1850
Bellazzini M., Ferraro F. R., Pancino E., 2001, ApJ, 556, 635
Bertin E., Arnouts S., 1996, A&AS, 117, 393
Bovy J., Rix H.-W., 2013, ApJ, 779, 115
Brown T. M., Smith E., Ferguson H. C., Rich R. M., Guhathakurta P., Renzini A., Sweigart A. V., Kimble R. A., 2006, ApJ, 652, 323
Bullock J. S., Johnston K. V., 2005, ApJ, 635, 931 (BJ05)
Calamida A. et al., 2014, ApJ, 790, 164
Carollo D. et al., 2007, Nature, 450, 1020
Carollo D. et al., 2010, ApJ, 712, 692
Carretta E., Gratton R. G., Clementini G., Fusi Pecci F., 2000, ApJ, 533, 215
Chabrier G., 2003, PASP, 115, 763
Cooper A. P. et al., 2010, MNRAS, 406, 744
D'Souza R., Kauffman G., Wang J., Vegetti S., 2014, MNRAS, 443, 1433
Dalcanton J. J. et al., 2012, ApJS, 200, 18
Davidge T. J., 2010, ApJ, 725, 1342
de Jong R. S., 2008, MNRAS, 388, 1521
de Jong R. S. et al., 2007, ApJ, 667, L49
de Vaucouleurs G., 1964, ApJ, 139, 899
Deason A. J., Belokurov V., Evans N. W., Johnston K. V., 2013, ApJ, 763, 113
Dolphin A. E., 2000, PASP, 112, 1383
Dotter A., Sarajedini A., Anderson J., 2011, ApJ, 738, 74
Ellis S. C., Bland-Hawthorn J., 2007, MNRAS, 377, 815
Font A. S., Johnston K. V., Bullock J. S., Robertson B. E., 2006a, ApJ, 638, 585
Font A. S., Johnston K. V., Bullock J. S., Robertson B. E., 2006b, ApJ, 646, 886
Font A. S., McCarthy I. G., Crain R. A., Theuns T., Schaye J., Wiersma R. P. C., Dalla Vecchia C., 2011, MNRAS, 416, 2802
Gilbert K. M. et al., 2012, ApJ, 760, 76
Gilbert K. M. et al., 2014, ApJ, 796, 76
Girardi L., Groenewegen M. A. T., Hatziminaoglou E., da Costa L., 2005, A&A, 436, 895
Girardi L. et al., 2010, ApJ, 724, 1030
Gómez F. A., Coleman-Smith C. E., O'Shea B. W., Tumlinson J., Wolpert R. L., 2012, ApJ, 760, 112
Gonzaga S., 2012, The DrizzlePac Handbook. Space Telescope Science Institute, MD, USA
Greggio L., Rejkuba M., Gonzalez O. A., Arnaboldi M., Iodice E., Irwin M., Neeser M. J., Emerson J., 2014, A&A, 562, A73
Haario H., Laine M., Mira A., Saksman E., 2006, Stat. Comput., 16, 339
Harris W. E., Canterna R., 1979, ApJ, 231, L19
Hook R., Stoehr F., Krist J., 2008, Space Telesc. Eur. Coordinating Facility Newsl., 44, 11
Hoyle F., Schwarzschild M., 1955, ApJS, 2, 1
Huchtmeier W. K., Richter O.-G., 1989, A General Catalog of HI Observations of Galaxies. The Reference Catalog. Springer-Verlag, Berlin
Ibata R. A. et al., 2014, ApJ, 780, 128
Ishigaki M. N., Chiba M., Aoki W., 2012, ApJ, 753, 64
Ivezić Ž. et al., 2008, ApJ, 684, 287
Janesh W. et al., 2015, preprint (arXiv:1503.09133)
Jang I. S., Lim S., Park H. S., Lee M. G., 2012, ApJ, 751, L19
Jarrett T. H., Chester T., Cutri R., Schneider S. E., Huchra J. P., 2003, AJ, 125, 525
Kauffmann G. et al., 2003, MNRAS, 341, 33
Krist J., 1995, in Shaw R. A., Payne H. E., Hayes J. J. E., eds, ASP Conf. Ser. Vol. 77, Astronomical Data Analysis Software and Systems IV. Astron. Soc. Pac., San Francisco, p. 349
Krist J. E., Hook R. N., Stoehr F., 2011, in Kahan M. A., ed., Proc. SPIE Conf. Ser. Vol. 8127, Optical Modeling and Performance Predictions V. SPIE, Bellingham, p. 81270J
McConnachie A. W. et al., 2009, Nature, 461, 66
Makarov D., Prugniel P., Terekhova N., Courtois H., Vauglin I., 2014, A&A, 570, A13
Malin D. F., Carter D., 1980, Nature, 285, 643
Malin D., Hadley B., 1997, PASA, 14, 52
Marigo P., Girardi L., Bressan A., Groenewegen M. A. T., Silva L., Granato G. L., 2008, A&A, 482, 883
Martínez-Delgado D. et al., 2010, AJ, 140, 962
Monachesi A., Trager S. C., Lauer T. R., Hidalgo S. L., Freedman W., Dressler A., Grillmair C., Mighell K. J., 2012, ApJ, 745, 97
Monachesi A. et al., 2013, ApJ, 766, 106
Monachesi A. et al., 2014, ApJ, 780, 179
Mouhcine M., Ibata R., 2009, MNRAS, 399, 737
Mouhcine M., Ferguson H. C., Rich R. M., Brown T. M., Smith T. E., 2005a, ApJ, 633, 810
Mouhcine M., Ferguson H. C., Rich R. M., Brown T. M., Smith T. E., 2005b, ApJ, 633, 821
Mouhcine M., Rich R. M., Ferguson H. C., Brown T. M., Smith T. E., 2005c, ApJ, 633, 828
Mouhcine M., Ibata R., Rejkuba M., 2010, ApJ, 714, L12
Okamoto S., Arimoto N., Ferguson A. M. N., Bernard E. J., Irwin M. J., Yamada Y., Utsumi Y., 2015, ApJ, 809, L1
Pietrinferni A., Cassisi S., Salaris M., Castelli F., 2004, ApJ, 612, 168
Pillepich A. et al., 2014, MNRAS, 444, 237
Pillepich A., Madau P., Mayer L., 2015, ApJ, 799, 184
Radburn-Smith D. J. et al., 2011, ApJS, 195, 18 (R-S11)
Radburn-Smith D. J. et al., 2014, ApJ, 780, 105
Renda A., Kawata D., Fenner Y., Gibson B. K., 2005a, MNRAS, 356, 1071

Renda A., Gibson B. K., Mouhcine M., Ibata R. A., Kawata D., Flynn C., Brook C. B., 2005b, MNRAS, 363, L16
Richardson J. C. et al., 2008, AJ, 135, 1998
Rizzi L., Tully R. B., Makarov D., Makarova L., Dolphin A. E., Sakai S., Shaya E. J., 2007, ApJ, 661, 815
Robertson B., Bullock J. S., Font A. S., Johnston K. V., Hernquist L., 2005, ApJ, 632, 872
Robin A. C., Reylé C., Derrière S., Picaud S., 2003, A&A, 409, 523
Sandage A., Smith L. L., 1966, ApJ, 144, 886
Sarajedini A. et al., 2007, AJ, 133, 1658
Sarajedini A., Yang S.-C., Monachesi A., Lauer T. R., Trager S. C., 2012, MNRAS, 425, 1459
Schaye J. et al., 2015, MNRAS, 446, 521
Schechtman-Rook A., Bershady M. A., 2013, ApJ, 773, 45
Schlafly E. F., Finkbeiner D. P., 2011, ApJ, 737, 103
Schlegel D. J., Finkbeiner D. P., Davis M., 1998, ApJ, 500, 525
Schönrich R., Asplund M., Casagrande L., 2011, MNRAS, 415, 3807
Sesar B., Jurić M., Ivezić Ž., 2011, ApJ, 731, 4
Sick J., Courteau S., Cuillandre J.-C., Dalcanton J., de Jong R., McDonald M., Simard D., Tully R. B., 2015, in Cappellari M., Courteau S., eds, Proc. IAU Symp. 311, Galaxy Masses as Constraints of Formation Models. Cambridge Univ. Press, Cambridge, p. 82
Slater C. T. et al., 2014, ApJ, 791, 9
Streich D., de Jong R. S., Bailin J., Goudfrooij P., Radburn-Smith D., Vlajic M., 2014, A&A, 563, A5
Streich D., de Jong R. S., Bailin J., Bell E. F., Holwerda B. W., Minchev I., Monachesi A., adburn-Smith D. J., 2016, A&A, 585, A97
Tissera P. B., Scannapieco C., Beers T. C., Carollo D., 2013, MNRAS, 432, 3391
Tissera P. B., Beers T. C., Carollo D., Scannapieco C., 2014, MNRAS, 439, 3128
Tumlinson J., 2010, ApJ, 708, 1398
van der Kruit P. C., 1984, A&A, 140, 470
van Dokkum P. G., Abraham R., Merritt A., 2014, ApJ, 782, L24
Vargas L. C., Gilbert K. M., Geha M., Tollerud E. J., Kirby E. N., Guhathakurta P., 2014, ApJ, 797, L2
Venn K. A., Irwin M., Shetrone M. D., Tout C. A., Hill V., Tolstoy E., 2004, AJ, 128, 1177
Wainscoat R. J., Hyland A. R., Freeman K. C., 1990, ApJ, 348, 85
White S. D. M., Rees M. J., 1978, MNRAS, 183, 341
Williams B. F. et al., 2014, ApJS, 215, 9
Worthey G., 1994, ApJS, 95, 107
Xue X.-X., Rix H.-W., Ma Z., Morrison H., Bovy J., Sesar B., Janesh W., 2015, ApJ, 809, 144
Zheng Z. et al., 1999, AJ, 117, 2757
Zhu C., Byrd R. H., Nocedal J., 1997, ACM Trans. Math. Softw., 23, 550
Zibetti S., White S. D. M., Brinkmann J., 2004, MNRAS, 347, 556

APPENDIX A: INFORMATION ABOUT EACH NEW INDIVIDUAL FIELD AND DOLPHOT PARAMETERS

We present in Table A1 relevant information regarding each field observed for the GHOSTS galaxies studied in this work. Some of those fields were already introduced in R-S11 (indicated with footnote *a*).

Table A2 indicates the DOLPHOT processing parameters that were used in the GHOSTS pipeline when running DOLPHOT through all the data. The only difference in the inputs between ACS and WFC3 data is the PSF. Tiny Tim synthetic PSFs (Krist 1995; Hook et al. 2008; Krist et al. 2011) were used for ACS data whereas Jay Anderson PSFs (ISR ACS 2006-01) were used for the WFC3 data. As explained above, we find that using Anderson PSFs on WFC3 data reduced the systematic offsets between the magnitudes of coincident stars in overlapping regions (see Williams et al. 2014, for a discussion on systematics due to PSF).

APPENDIX B: AUTOMATED SELECTION CRITERIA DETERMINATION FOR WFC3 FIELDS

We describe here the method employed for determining the best selection criteria, i.e. 'photometry culls', in order to reduce at maximum the unresolvable background galaxies that appear as detections in the WFC3 DOLPHOT photometric outputs. At the same time, the culls must have minimal impact on the true stellar detections. The method employed for determining the ACS culls is described in R-S11.

We used several deep WFC3/UVIS exposures of five fields from the *HST* archive that are far from any nearby galaxy, and thus we call 'empty' archival WFC3 fields (see Table B1). These observations should be free of resolvable stars others than the MW foreground stars. We chose exposures that have similar exposures times to our observed data and thus are ideal for understanding the background galaxy contaminants of our fields. We ran DOLPHOT on these 'empty' fields using the same processing parameters as those used on the GHOSTS observations, indicated in Table A2. We then re-ran DOLPHOT after injecting ∼300 000 artificial stars in them, distributed approximately to recreate a typical GHOSTS CMD.

Having the DOLPHOT outputs from both the 'empty' archival fields and the ASTs on those fields, we ran a Metropolis–Hasting type Markov Chain Monte Carlo (MCMC) algorithm (Haario et al. 2006) over a range of possible selection criteria that we apply to both the empty field detections and AST output. The MCMC code then searches to minimize the number of unresolved galaxies that pass the culls while maximizing the number of artificial stars that pass the same culls. Specifically, the MCMC code minimizes the negative log-likelihood function:

$$\mathcal{L} = -1/2 \times (a^2 + b^2), \tag{B1}$$

where a as the fraction of artificial stars that fails to pass the culls and b the fraction of detections in the archival fields that passed the culls in each field. The range of possible selection criteria was chosen based on our experience with ACS culls (see R-S11). We search for values that are close to the ACS culls, which used parameters from the DOLPHOT diagnostic output described in Section 3. The final selection criteria for WFC3 fields, or 'WFC3 culls' are

$$-0.19 < \mathrm{sharpness}_{F606W} + \mathrm{sharpness}_{F814W} < 1.50$$

$$\mathrm{crowding}_{F606W} + \mathrm{crowding}_{F814W} < 0.20$$

$$\mathrm{S/N}_{F606W} > 5.1, \mathrm{S/N}_{\mathrm{F814W}} > 3.2.$$

In addition, we select detections for which DOLPHOT reports an object type 1, which indicates a clean point source, as well as an error flag of 2 or less, which indicates that there are not many bad or saturated pixels.

The effect of the WFC3 culls can be seen in Fig. B1. The top panels in this figure show the CMDs of DOLPHOT detections after performing photometry on the empty fields. The sources in these CMDs are mostly unresolved background galaxies and some foreground MW stars. The bottom panels show the CMDs after the WFC3 culls have been applied to the source catalogues of the same fields. Foreground MW stars remain as well as some unresolved background galaxies that passed the culls. After applying the selection criteria on the empty fields, ∼95 per cent of the contaminants have been removed. Note that the number of unresolved galaxies that remain fluctuates slightly from field to field depending mainly on the exposure time of the observations.

Table A1. Information on each field of the *HST*/ACS *HST*/WFC3 observations.

Galaxy	Field	Proposal ID	α_{2000} (°)	δ_{2000} (°)	Position angle	Observation date	Camera	t_{F606W} (s)	t_{F814W} (s)
(1)	(2)	(3)	(4)	(5)	(6)	(7)	(8)	(9)	(10)
NGC 0253	Field-01[a]	10915	11.9013	−25.2789	139.99	2006-09-13	ACS	1508(2)	1534(2)
	Field-02[a]	10915	11.9461	−25.2457	140.89	2006-09-09	ACS	1508(2)	1534(2)
	Field-03[a]	10915	11.9908	−25.2126	159.21	2006-09-15	ACS	1508(2)	1534(2)
	Field-04[a]	10915	12.0356	−25.1794	139.99	2006-09-08	ACS	1508(2)	1534(2)
	Field-05[a]	10915	12.0803	−25.1463	144.99	2006-09-19	ACS	2283(3)	2253(3)
	Field-06[a]	10523	12.1479	−25.0881	51.04	2006-05-19	ACS	680(2)	680(2)
	Field-07[a]	10523	12.2311	−25.0104	113.60	2005-09-01	ACS	680(2)	680(2)
	Field-08[a]	10523	11.8080	−25.1696	60.16	2006-06-13	ACS	680(2)	680(2)
	Field-09[a]	10523	11.9376	−25.3697	134.79	2005-09-13	ACS	680(2)	680(2)
	Field-10[a]	10523	11.8456	−25.4283	190.72	2005-10-24	ACS	680(2)	680(2)
	Field-11	12213	11.6372	−25.0007	256.45	2010-12-18	WFC3	1076(2)	1219(2)
	Field-12	12213	11.6034	−24.9781	256.45	2010-12-18	ACS	843(2)	1182(2)
	Field-13	11613	11.5346	−24.8585	60.75	2010-06-11	ACS	800(2)	680(2)
	Field-14	11613	11.4304	−24.8312	60.75	2010-06-11	WFC3	725(1)	1175(2)
	Field-15	12213	11.3479	−24.6810	234.97	2010-11-04	WFC3	1076(2)	1218(2)
	Field-16	12213	11.3074	−24.6711	234.97	2010-11-04	ACS	842(2)	1182(2)
	Field-17	12213	11.2291	−24.5825	240.26	2010-11-18	WFC3	1076(2)	1218(2)
	Field-18	12213	11.1897	−24.5693	240.26	2010-11-18	ACS	842(2)	1182(2)
	Field-19	12213	11.0445	−24.3522	234.97	2010-11-04	WFC3	1076(2)	1218(2)
	Field-20	12213	11.0041	−24.3424	234.97	2010-11-04	ACS	842(2)	1182(2)
NGC 0891	Field-01[a]	9414	35.6779	42.3283	243.99	2003-02-19	ACS	7711(9)	7711(9)
	Field-02[a]	9414	35.7070	42.3803	244.28	2004-01-17	ACS	7711(9)	7711(9)
	Field-03[a]	9765	35.6618	42.4043	244.01	2004-02-18	ACS	676(2)	700(2)
	Field-04[a]	9414	35.7358	42.4318	244.62	2004-02-17	ACS	7711(9)	7711(9)
	Field-05[a]	10889	35.6523	42.3473	17.23	2006-10-22	ACS	3170(3)	3080(3)
	Field-06	12213	35.7843	42.3048	246.63	2011-02-12	ACS	2506(6)	3366(6)
	Field-07	12213	35.8278	42.2970	246.63	2011-02-12	WFC3	2890(6)	4032(6)
	Field-08	12213	36.0332	42.2355	246.72	2011-02-12	ACS	2100(5)	2740(5)
	Field-09	12213	36.0767	42.2277	246.72	2011-02-12	WFC3	1786(4)	2688(4)
	Field-10	12196	35.6612	42.3940	337.99	2011-11-08	WFC3	3134(2)	4754(6)
	Field-11	12196	35.6845	42.4359	337.99	2011-11-08	WFC3	3134(6)	4754(6)
	Field-12	12196	35.6612	42.3940	337.99	2011-11-08	ACS	3471(6)	3647(6)
	Field-13	12196	35.6845	42.4359	337.99	2011-11-08	ACS	3471(6)	3647(6)
NGC 3031	Field-01[a]	9353	148.8541	69.0202	272.79	2002-05-28	ACS	834(2)	1671(3)
	Field-02[a]	10915	148.6446	69.2804	89.81	2006-11-16	ACS	24232(10)	29953(12)
	Field-03[a]	10523	148.5963	69.3323	84.98	2005-12-06	ACS	700(2)	700(2)
	Field-04[a]	10523	148.4984	69.4162	120.25	2005-10-26	ACS	720(2)	720(2)
	Field-05[a]	10523	149.3217	69.1081	117.08	2005-10-31	ACS	710(2)	710(2)
	Field-06[a]	10523	149.5187	69.1478	117.32	2005-10-31	ACS	735(2)	735(2)
	Field-07[a]	10523	149.7178	69.1783	162.14	2005-09-07	ACS	730(2)	730(2)
	Field-08[a]	10523	149.1630	69.3748	70.08	2005-12-20	ACS	740(2)	740(2)
	Field-09[a]	10136	148.5689	69.0932	297.00	2005-04-13	ACS	5354(4)	5501(4)
	Field-10[a]	10584	149.1176	68.9110	69.76	2005-12-09	ACS	1580(3)	1595(3)
	Field-11[a]	10584	149.2538	68.9315	69.76	2005-12-06	ACS	1580(3)	1595(3)
	Field-12[a]	10604	148.2633	68.8676	160.11	2005-09-11	ACS	12470(10)	22446(18)
	Field-13	11613	148.5480	69.4435	266.00	2010-06-03	WFC3	735(1)	1225(2)
	Field-14	11613	148.3369	69.5085	266.00	2010-06-03	ACS	850(2)	690(2)
	Field-15	11613	148.3377	69.6583	219.74	2010-07-16	WFC3	735(1)	1225(2)
	Field-16	11613	148.0555	69.6497	219.74	2010-07-16	ACS	850(2)	690(2)
	Field-17	11613	147.9212	69.7207	40.64	2009-12-31	ACS	830(2)	680(2)
	Field-18	11613	147.6379	69.7141	40.64	2009-12-31	WFC3	725(1)	1200(2)
	Field-19	11613	149.7859	69.2047	35.13	2010-01-18	WFC3	735(1)	1225(2)
	Field-20	11613	150.0595	69.2207	35.13	2010-01-18	ACS	850(2)	690(2)
	Field-21	11613	150.3768	69.2199	356.93	2010-02-25	WFC3	725(1)	1200(2)
	Field-22	11613	150.3953	69.2675	215.87	2010-07-22	ACS	850(2)	690(2)
	Field-23	11613	150.4575	69.3234	49.55	2010-01-23	WFC3	735(1)	1225(2)
	Field-24	11613	150.5644	69.2926	356.93	2010-02-25	ACS	830(2)	680(2)
	Field-25	11613	150.670	69.2827	215.87	2010-07-22	WFC3	735(1)	1225(2)
	Field-26	11613	150.7350	69.3147	49.55	2010-01-23	ACS	850(2)	690(2)
	Field-27	11613	147.7289	68.8632	108.28	2009-11-09	WFC3	735(1)	1225(2)
	Field-28	11613	147.8496	68.7749	108.28	2009-11-09	ACS	850(2)	690(2)

Table A1 – *continued*

Galaxy	Field	Proposal ID	α_{2000} (°)	δ_{2000} (°)	Position angle	Observation date	Camera	t_{F606W} (s)	t_{F814W} (s)
(1)	(2)	(3)	(4)	(5)	(6)	(7)	(8)	(9)	(10)
NGC 4565	Field-01[a]	10889	189.1069	26.0161	119.15	2006-12-13	ACS	7350(7)	7192(7)
	Field-02[a]	10889	189.1499	25.9707	118.00	2006-12-15	ACS	7350(7)	7192(7)
	Field-03[a]	10889	189.1703	26.0700	118.78	2006-12-14	ACS	7350(7)	7192(7)
	Field-04[a]	9765	189.0306	26.0324	337.78	2004-04-15	ACS	676(2)	700(2)
	Field-05	12213	189.2549	26.1107	336.98	2011-04-21	WFC3	7763(7)	10479(7)
	Field-06	12213	189.2810	26.1556	336.98	2011-04-21	ACS	8883(7)	7878(7)
	Field-07	12196	188.9776	26.1016	100.97	2011-01-24	ACS	8265(6)	7340(6)
	Field-08	12196	188.9776	26.1016	100.97	2011-01-24	WFC3	5795(5)	9880(6)
NGC 4945	Field-01	11613	196.5884	−49.3066	155.49	2010-03-17	ACS	830(2)	680(2)
	Field-02	11613	196.6422	−49.2146	155.49	2010-03-17	WFC3	725(1)	1205(2)
	Field-03	11613	196.7622	−49.1803	275.91	2010-06-24	ACS	830(2)	680(2)
	Field-04	11613	196.8563	−49.2572	275.91	2010-06-24	WFC3	725(1)	1205(2)
	Field-05	11613	196.9382	−49.0558	157.13	2010-03-20	ACS	830(2)	680(2)
	Field-06	11613	196.9957	−48.9649	157.13	2010-03-20	WFC3	725(1)	1205(2)
	Field-07	11613	196.1443	−49.4310	315.79	2010-08-25	WFC3	725(1)	1170(2)
	Field-08	11613	196.1474	−49.3325	315.79	2010-08-25	ACS	800(2)	680(2)
	Field-09	11613	196.0315	−49.3653	318.17	2010-08-28	WFC3	725(1)	975(1)
	Field-10	11613	196.0418	−49.2676	318.17	2010-08-28	ACS	830(2)	680(2)
	Field-11	11613	195.8408	−49.1319	263.61	2010-06-08	WFC3	725(1)	1170(2)
	Field-12	11613	195.7240	−49.0698	263.61	2010-06-08	ACS	800(2)	680(2)
NGC 7814	Field-01[a]	10889	0.8017	16.1263	30.15	2006-08-26	ACS	5211(5)	5215(5)
	Field-02[a]	10889	0.8512	16.0994	25.98	2006-09-13	ACS	5211(5)	5215(5)
	Field-03[a]	10889	0.7976	16.1451	46.96	2006-07-24	ACS	5211(5)	5215(5)
	Field-04[a]	10889	0.7468	16.0699	27.99	2006-09-12	ACS	5211(5)	5215(5)
	Field-05[a]	10889	0.8139	16.0715	22.98	2006-09-15	ACS	5211(5)	5215(5)
	Field-06	12213	0.6484	15.9835	339.98	2010-09-29	ACS	9656(8)	8108(8)
	Field-07	12213	0.6105	15.9126	339.98	2010-09-29	WFC3	8348(8)	11088(8)

[a]Field presented in R-S11.

Notes. (1) NGC identifier; (2) field number. Fields are numerically labelled outwards following the identification in R-S11, i.e. first along one side of the major axis, then along one side of the minor axis, then any axis in between the major and minor before labelling the remaining fields by distance from the galaxy centre; (3) *HST* Proposal ID of the observation; (4) and (5) right ascension and declination in degrees; (6) the *HST* PA_V3 angle, which records the projected angle on the sky eastwards of north that the observatory was rotated; (7) observation date; (8) *HST* camera; (9) and (10) the total time of the exposures in seconds for the *F*606*W* and F814W filters. The number of exposures observed in each filter is indicated in brackets.

APPENDIX C: TRGB DISTANCES OF ALL GHOSTS GALAXIES

We derive the TRGB distances of NGC 4945, NGC 0247, NGC 4631, and NGC 5023. NGC 4945 and NGC 0247 were not in the sample of GHOSTS galaxies presented in R-S11 and therefore we measure their TRGB distances for the first time. We re-measure the distances to NGC 4631 and NGC 5023 because our previous observations have only fields on top of their discs and the severe crowding as well as the high contamination from younger more metal-rich stars prohibited an accurate measurement of the TRGB apparent magnitude. The new data for these galaxies have fields further out from their discs and allow us to get a better estimate of such measurement. We detect the TRGB for fields with enough stars within 0.2 mag of the TRGB and that are not heavily contaminated by young stars as well as not too crowded.

As mentioned in Section 4, the *I* magnitude of the TRGB is almost constant for old populations with metallicities [Fe/H] < -0.7 only weakly dependent on metallicity, providing the best way to derive distances to nearby galaxies. The metallicity dependence, however, can be identified using the colour of TRGB stars (Bellazzini et al. 2001). Rizzi et al. (2007), used *HST* observations of five Local Group galaxies to calibrate the TRGB absolute magnitude as a function of TRGB colour. They have scaled the apparent magnitude of the TRGB to an assumed luminosity for the horizontal branch, whose absolute magnitude depends on metallicity (Carretta et al. 2000), and obtained the following relation that we use to determine the TRGB absolute magnitude:

$$M_{F814W} = -4.06 + 0.20[(F606W - F814W) - 1.23]. \quad \text{(C1)}$$

We measure the apparent magnitude of the TRGB following a method similar to that of Makarov et al. (2006), but simultaneously fitting multiple fields for each galaxy. In this method, an unbinned maximum likelihood fit is performed to the *F*814*W* luminosity function (LF) near the visually estimated TRGB. The model LF for all stars is a weighted sum of the model LF for each field, which consists of two power laws joined together at a discontinuous jump convolved with a magnitude-dependent Gaussian whose width and zero-point correspond to the photometric uncertainty in that field. Formally, if the array of LF parameters is $\boldsymbol{x} = (m_{\rm TRGB}, a, b, c)$, then the model LF $\varphi(m)$ is

$$\varphi(m|\boldsymbol{x}) = \sum_f k_f \, \varphi_f(m|\boldsymbol{x}), \quad \text{(C2)}$$

where the individual field model LF for field f is

$$\varphi_f(m|\boldsymbol{x}) = \int \psi(m'|\boldsymbol{x}) \, e_f(m|m') \, \mathrm{d}m', \quad \text{(C3)}$$

Table A2. DOLPHOT processing parameters.

Description	Parameter	Value
Photometry aperture size	RAper	3
Photometry type	PSFPhot	1
Fit sky?	FitSky	2
Inner sky radius	RSky0	15
Outer sky radius	RSky1	35
χ-statistic aperture size	Rchi	2.0
Spacing for sky measurement	SkipSky	2
Sigma clipping for sky	SkySig	2.25
Second pass finding stars	SecondPass	5
Searching algorithm	SearchMode	1
Sigma detection threshold	SigFind	2.5
Multiple for quick-and-dirty photometry	SigFindMult	0.85
Sigma output threshold	SigFinal	3.5
Maximum iterations	MaxIT	25
Noise multiple in imgadd	NoiseMult	0.10
Fraaction of saturate limit	FSat	0.999
Find/make aperture corrections?	ApCor	1
Force type 1/2?	Force1	0
Use WCS for initial alignment?	useWCS	1
Align images?	Align	4
Allow cross terms in alignment?	Rotate	1
Centroid box size	RCentroid	1
Search step for position iterations	PosStep	0.25
Maximum single-step in position iterations	dPosMax	2.5
Minimum separation for two stars for cleaning	RCombine	1.415
PSF size	RPSF	10
Minimum S/N for PSF parameter fits	SigPSF	3.0
Make PSF residual image?	PSFres	1
Coordinate offset	Psfoff	0.0
Flag setting to remove poor objects from final phot	FlagMAsk	4
Use the DOLPHOT CTE correction	UseCTE	0

Table B1. Empty WFC3 archival fields.

Field number	PID	l (°)	b (°)	t_{F606W} (s)	t_{F814W} (s)
1	13352	200.56	−30.41	2500	2500
2	13352	9.94	+41.97	1200	1650
3	13352	302.55	+60.52	2400	2400
4	13352	223.73	+29.15	2200	2200

the theoretical LF is

$$\psi(m|\boldsymbol{x}) = \begin{cases} 10^{a(m-m_{\rm TRGB})+b} & m \geq m_{\rm TRGB} \\ 10^{c(m-m_{\rm TRGB})} & m < m_{\rm TRGB}, \end{cases} \quad \text{(C4)}$$

and the Gaussian error kernel for field f is

$$e_f(m|m') = \frac{1}{\sqrt{2\pi}\sigma_f(m')} \mathrm{e}^{-\frac{1}{2}[m-\bar{m}_f(m')]^2/\sigma_f^2}. \quad \text{(C5)}$$

The photometric uncertainty $\sigma_f(m)$ and the median output magnitude $\bar{m}_f(m)$ at $F814W{=}m$ were derived from exponential fits to the AST results for field f over the range $22 \leq F814W \leq 26$. Note that unlike Makarov et al. (2006), we neglect the completeness, which is negligible due to the depth of the data.

The weights normalize the model LFs to the number of observed stars near the TRGB in each field, and are formally defined as

$$k_f = \frac{N_f}{\int \varphi_f(m|\boldsymbol{x})\,\mathrm{d}m}, \quad \text{(C6)}$$

where N_f is the number of selected stars in field f.

Stars were selected within ± 1 mag of an initial $m_{\rm TRGB}$ estimate, and which satisfied a colour cut to remove both blue MS and redder AGB stars. For most fields, the colour cut was $0.3 < F606W - F814W < 1.6$, but colours redder than 0.3 were required as the lower limit in some fields that were particularly metal rich, or where helium-burning sequences were prominent, and a colour bluer than 1.6 was required as the upper limit in NGC 4945 due to foreground contamination.

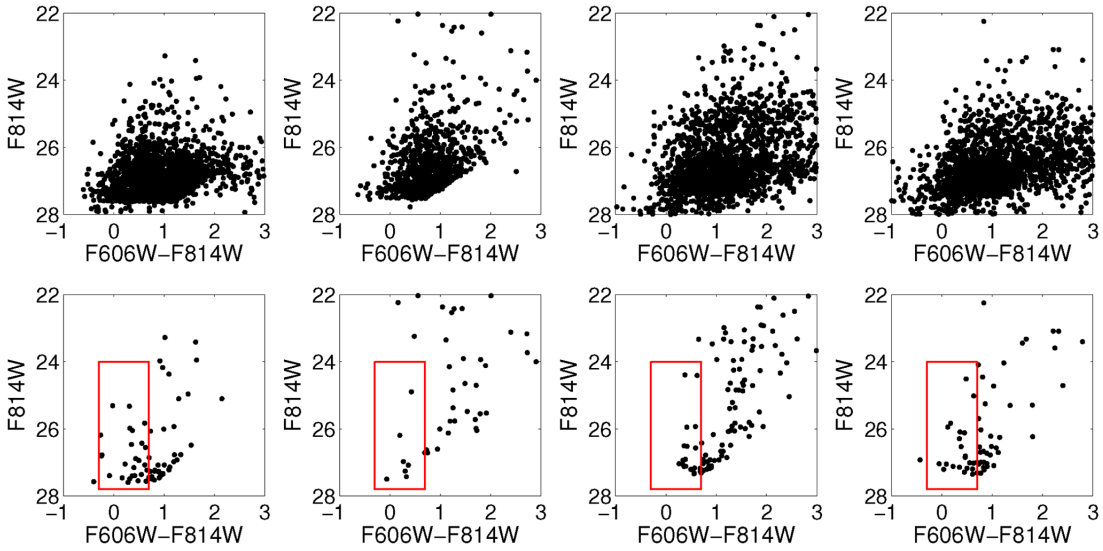

Figure B1. Results from applying the WFC3 culls to the empty archival fields. The top panels show the CMDs of detections obtained from DOLPHOT on empty WFC3 archival fields. Most of these detections are unresolved background galaxies that occupy the RGB region of the field galaxies, mostly contaminating the more distant galaxies whose TRGBs are fainter than $F814W \sim 25.5$. The bottom panels show the CMDs after the final WFC3 culls have been applied. Foreground MW stars remain as well as some background galaxies that passed the culls. Red boxes indicate the region between colours −0.2 and 0.75. Galaxies such as NGC 4565 and NGC 7814 have detections that passed the culls within these colours, which may be due to remaining background galaxies/quasars.

Table C1. TRGB distances to all galaxies in the GHOSTS survey obtained in this work and in R-S11.

Name	$F814W_{\rm TRGB}$ (VEGAmag)	$(F606W-F814W)_{\rm TRGB}$ (VEGAmag)	$(m-M)_{\rm TRGB}$ (mag)	D (Mpc)
(1)	(2)	(3)	(4)	(5)
NGC 0247	$23.76^{+0.012}_{-0.008}$	1.25 ± 0.35	27.82 ± 0.07	3.66 ± 0.1
NGC 0253[a]	23.65 ± 0.03	1.26 ± 0.20	27.70 ± 0.07	3.50 ± 0.1
NGC 0891[a]	25.76 ± 0.03	1.34 ± 0.25	29.80 ± 0.09	9.1 ± 0.4
NGC 2403[a]	23.43 ± 0.02	1.14 ± 0.10	27.51 ± 0.07	3.2 ± 0.1
NGC 3031[a]	23.71 ± 0.02	1.14 ± 0.15	27.79 ± 0.07	3.6 ± 0.1
NGC 4244[a]	24.12 ± 0.02	1.09 ± 0.10	28.21 ± 0.11	4.4 ± 0.2
NGC 4565[a]	26.32 ± 0.02	1.25 ± 0.21	30.38 ± 0.05	$11.9^{+0.3}_{-0.2}$
NGC 4631	$25.29^{+0.007}_{-0.009}$	1.15 ± 0.50	29.36 ± 0.15	7.46 ± 0.5
NGC 4736[a]	24.21 ± 0.03	1.90 ± 0.50	28.14 ± 0.13	4.2 ± 0.3
NGC 4945	$23.72^{+0.014}_{-0.016}$	1.35 ± 0.50	27.76 ± 0.12	3.56 ± 0.2
NGC 5023	$24.99^{+0.015}_{-0.016}$	1.16 ± 0.33	29.06 ± 0.07	6.5 ± 0.2
NGC 5236[a]	24.38 ± 0.03	1.25 ± 0.30	28.41 ± 0.11	4.8 ± 0.2
NGC 5907[a]	27.05 ± 0.04	1.14 ± 0.29	31.13 ± 0.1	$16.8^{+0.8}_{-0.7}$
NGC 7793[a]	23.79 ± 0.03	1.15 ± 0.13	27.87 ± 0.08	3.7 ± 0.1
NGC 7814[a]	26.74 ± 0.03	1.27 ± 0.25	30.80 ± 0.10	$14.4^{+0.7}_{-0.6}$
IC 5052[a]	24.72 ± 0.05	1.34 ± 0.22	28.76 ± 0.1	$5.6^{+0.3}_{-0.2}$

[a]TRGB distance calculated by R-S11.

Notes. (1) NGC identifier; (2) averaged values of the TRGB magnitude are listed using the individual TRGB detections of each field used per galaxy, except for IC 5052 and NGC 7793, where the TRGB detection has been done for only one field, and for the TRGB magnitudes derived in this work which are calculated using information about all fields used (see text for a detailed description). The uncertainties on these fields are combined in quadrature for each galaxy, and where three or more measurements exist this is also combined in quadrature with an estimate of the standard deviation of the results; (3) averaged values of the colour at the TRGB using the colour estimate per field. Each field colour at the TRGB is estimated by fitting a Gaussian to the distribution of stars within 0.2 mag of the TRGB, and errors are the width of the Gaussian fitted across the distributions. The uncertainties on these measurements are combined in quadrature for each galaxy, and where three or more measurements exist this is also combined in quadrature with an estimate of the standard deviation of the results; (4) the distance modulus calculated using the detection in Column 2, the colour in Column 3 and equation (C1). The reported error incorporates the errors both in the TRGB magnitude and the colour; (5) distance to the galaxy in Mpc using Column 4.

The maximum likelihood fit to the LF was determined by minimizing the negative log-likelihood function

$$\mathcal{L}(\boldsymbol{x}) = -\sum_i \ln \varphi(m_i|\boldsymbol{x}) + N \ln \int \varphi(m|\boldsymbol{x})\,{\rm d}m, \qquad \text{(C7)}$$

with respect to the parameters $\boldsymbol{x}$. The integrals in equations (C6) and (C7) are over the 2 mag selected magnitude range, and N is the total number of selected stars. Minimization was performed via the L-BFGS-B algorithm (Zhu, Byrd & Nocedal 1997), which is good for general-purpose minimization and allows for bounded solutions to prevent $m_{\rm TRGB}$ from becoming unphysical.

The uncertainty in the TRGB magnitude was calculated as the 16th and 84th percentiles of 500 bootstrap resamplings of the CMD. Table C1 provides the TRGB distances to all GHOSTS galaxies. The galaxies for which their TRGB distances have been measured by R-S11 are indicated with superscript *a*.

APPENDIX D: POSSIBLE SYSTEMATIC BIASES DUE TO VARYING THE SELECTION BOXES

As presented in Section 5.1, the selection boxes differ from galaxy to galaxy. The different selection boxes can be divided in two types; one that spans a large range in $F814W$ magnitudes, between ∼1.5 and ∼2 mag below the TRGB for the three closer galaxies NGC 0253, NGC 3031, and NGC 4945. The second selection box covers a much smaller range of $F814W$ magnitudes, between ∼0.5 and ∼0.7 mag below the TRGB for the three more distant galaxies NGC 0891, NGC 4565, and NGC 7814. The differences in the selection boxes might be introducing systematic biases affecting the resulting colour measurements, and therefore the colour profiles. This may be a concern especially since the galaxies that show flat colour profiles are the same ones for which a larger sample of RGB stars was used to estimate the measured quantities.

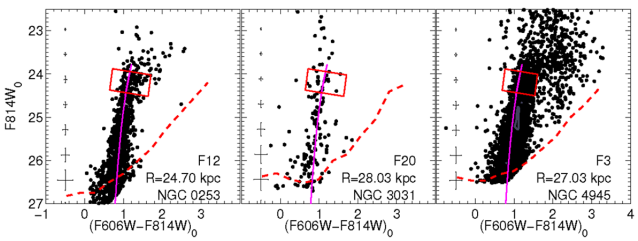

Figure D1. CMDs of one field in NGC 0253 (left), NGC 3031(middle), and NGC 4945 (right) showing the smaller selection box used here in order to test for possible systematic biases. This selection box is the one used in Section 5 for NGC 7814 and it is nearly the same as the one used for NGC 0891 and NGC 4565.

There are two possible systematic biases on the measured colours and colour distributions that could be introduced by the differences in the selection boxes. First, the smaller selection boxes implies measuring stars within a smaller range of magnitudes below the

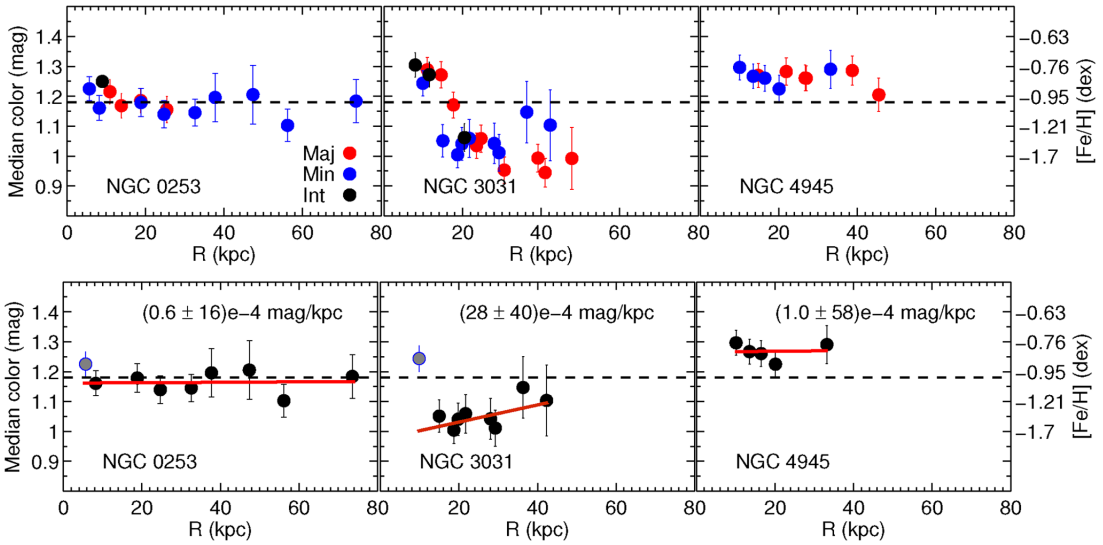

Figure D2. Colour profiles of NGC 0253 (left), NGC 3031 (middle), and NGC 4945 (right) obtained using the same smaller selection box, with stars selected within 0.5 mag below the TRGB. Top panels: global colour profiles, i.e. using all the available fields. Red, blue, and black dots indicate fields along the major, minor and intermediate axis, respectively. To be compared with Fig. 11. Bottom panels: stellar halo colour profiles, using only fields along the minor axis. We find no significant differences in these colour profiles with those shown in Fig. 12 for these galaxies. In particular, no negative gradient is found when the smaller selection boxes are used. There is however a redder colour in the outer fields of NGC 3031, along the minor axis, which may be indicative of halo substructure.

TRGB. This is the most sensitive RGB region to metallicity variation and therefore where the RGB is broadest if there is a wide range of metallicities in the stellar population. Given the steep luminosity function of the RGB, the detection of a weak gradient may be hidden if a larger magnitude range of RGB stars is used, as in the case of the larger selection boxes. Second, the fainter reddest boundaries of the smaller boxes are very close to the 70 per cent or even to 50 per cent completeness in some cases, whereas the boundaries of the larger boxes are above those completeness. This results in larger photometric uncertainties for the redder stars within the smaller selection boxes than for those selected within the larger selection boxes.

To test these possible biases, we construct the colour profiles presented in Figs 11 and 12 using the same small selection box for all galaxies. This selection box spans a magnitude range of 0.5 mag from the TRGB where there is a more sensitive metallicity variation with colour, however many fewer stars per field. This is especially so for the nearer galaxies, given the small physical area of each *HST* field on the sky. In order to use a statistical sample of stars to measure the median colour, we impose a minimum of 10 stars per selection box (see Section 5.2). When this is not reached in one field, we add together two fields in proximity, and along the same axis, and calculate the median colour and colour distribution of these two fields together instead. This was the case for the outer fields in NGC 0253 and NGC 3031.

We show in Fig. D1 the CMDs with the smaller selection boxes for NGC 0253, NGC 3031, and NGC 4945. We follow the exact same steps as in Section 5 using these new selected stars and obtain the median colours and colour distributions for these fields. The resulting colour profiles using all fields and stellar halo profiles using only the minor axis fields for these three galaxies are shown in Fig. D2. We only show these three galaxies since there is no difference in the profiles for the remaining galaxies, NGC 0891, NGC 4565, and NGC 7814. The smaller selection box used here is the box used in Section 5 for NGC 7814 and it is nearly identical as the selection box used for NGC 0891 and NGC 4565. Other than the larger uncertainties in the median colour values, due to the fewer number of stars used, and a somewhat redder colour in some of the fields, the colour profiles do not appear to show a negative gradient with radius. For NGC 3031, however, there seems to be a redder colour in the outer most fields along the minor axis, which might be due to substructure in the halo.

In addition, we have checked that the differences in completeness of our data does not have an impact in our results. When we use the same smaller selection box for all galaxies, the completeness of the stars in the closer galaxies within the smaller selection box is nearly 100 per cent whereas this is about 70 per cent or even 50 per cent for some stars within the selection box for the more distant galaxies. We have found no significant differences in the colour profiles when these are corrected for incompleteness.

Thus, we conclude that the results presented are not driven by the selection boxes.

This paper has been typeset from a TEX/LATEX file prepared by the author.